





High-precision photometric and high-resolution spectroscopic characterization of HD 180347

Otto Trust ¹★, Lyudmila Mashonkina ²★, Edward Jurua ¹★, Peter De Cat ³, Vadim Tsymbal² and Santosh Joshi⁴

¹Department of Physics, Mbarara University of Science and Technology, P.O. Box 1410, Mbarara, Uganda

²Institute of Astronomy, Russian Academy of Sciences, 119017, Pyatnitskaya str., 48, Moscow, Russia

³Royal Observatory of Belgium, Ringlaan 3, B-1180 Brussel, Belgium

⁴Aryabhata Research Institute of Observational Sciences, Manora Peak, Nainital- 263002, India

Accepted 2023 June 23. Received 2023 May 9; in original form 2023 February 2

ABSTRACT

We report the analysis of high-precision space-based photometric and high-resolution spectroscopic observations of HD 180347. The high-quality light curves from the *Transiting Exoplanet Survey Satellite* (*TESS*) under sectors 14, 15, and 26 were used. By visual inspection of the light curves and the Fourier transforms, only low-frequency signals (less than 1 d^{-1}) were detected. After using wavelet, autocorrelation, and composite spectrum analyses, HD 180347 is classified as a rotational variable with a period of about $4.1 \pm 0.2 \text{ d}$. In reference to the observation limit of *TESS*, no pulsations were detected. For the spectroscopic analysis, we used data collected with the High Efficiency and Resolution Mercator Échelle Spectrograph (HERMES). We determined the spectral type of this star and obtained atmospheric parameters such as the effective temperature, the surface gravity, and the projected rotational, microturbulent, and radial velocities. We performed a detailed chemical abundance analysis. The LTE abundances were derived for 25 chemical elements. For 13 of them, including Ca, Sc, Sr, Zr, and Ba, which are important for the characterization of chemical peculiarities, we also present the non-local thermodynamic equilibrium (NLTE) abundances. NLTE improves the accuracy of the derived abundances and confirms that Ca and Sc are depleted in HD 180347 relative to their solar abundances, while the heavy elements beyond Sr are enhanced, by more than 0.7 dex. Based on the spectral class and the element abundance pattern, we classify this star as Am (kA1hA8mA8).

Key words: stars: abundances – stars: chemically peculiar – stars: fundamental parameters – stars: rotation – starspots – stars: individual: HD 180347.

1 INTRODUCTION

Over 10 percent of the intermediate mass main-sequence stars (A- and F-type) are chemically peculiar (CP). The CP stars show anomalies in their chemical composition compared to the solar one. The CP stars are categorized into four major groups: CP1 stars (the metallic-line or Am/Fm stars), CP2 stars (the magnetic Ap stars), CP3 stars (the Mercury-Manganese or HgMn stars), and CP4 stars (the He-weak stars), based on their magnetic field and absorption line strengths (Preston 1974). The Am stars are distinguished by low abundances of some elements such as Ca and Sc, as well as an excess of Fe-group metals and often weak or absent magnetic fields (Conti 1970; Preston 1974; Romanyuk 2007). In the Am stars subgroup, the Ca II K-line appears too early compared to the types derived from hydrogen lines, whilst metallic lines appear too late, resulting in spectral types inferred from the Ca II K- and metal lines differing by five or more spectral subclasses. For the marginal Am stars, the spectral subclasses between the Ca II K- and metal lines are less than five. The frequently used detailed classification for this

class of objects involves three spectral subtypes prefixed with k, h, and m, which represent Ca II K-line, hydrogen lines, and metallic lines, respectively.

Some metals like Si, Cr, Sr, and Hg, as well as rare-earth elements like Eu, Nd, Pr, and others, are overabundant in the CP2 stars in comparison to solar values (Conti 1970; Preston 1974; Kurtz & Martinez 2000; Romanyuk 2007). Unlike CP1 and CP3, the presence of well-organized magnetic fields with strengths of several tens of kG is also a feature of CP2 stars (Aurière et al. 2007). In their spectra, the CP3 stars have amplified HgII (398.4 nm) and/or MnII lines, as well as faint lines of light elements (such as He, Al, and N). In the spectra of the CP4 stars, there are unusually weak HeI lines and these stars are characterized by magnetic fields with a strength of up to 1 kG (Jones & Wolff 1974; Preston 1974; Smith 1997; Bohlender, Dworetzky & Jomaron 1998). The CP stars are slow rotators with a projected rotational velocity ($v \sin i$) below 120 km s^{-1} (Abt 2009).

The interplay between radiative levitation and gravitational settling, known as atomic diffusion, is assumed to be the principal source of chemical anomalies in CP stars (Michaud 1970; Watson 1970; Khokhlova 1981; Hui-Bon-Hoa 2000; Richer, Michaud & Turcotte 2000; Turcotte 2003; Théado et al. 2011). In the absence of mixing, light elements sink under gravity and are perceived as underabundant, whereas heavy elements are radiatively forced outward and reflected

* E-mail: otrust@must.ac.ug (OT); lima@inasan.ru (LM); ejurua@must.ac.ug (EJ)

as overabundant. This idea necessitates calm and stable atmospheres, which are aided by CP stars' sluggish rotation behaviour (Fossati et al. 2008; Takeda et al. 2008; Abt 2009; Stateva et al. 2009) and Ap stars' strong magnetic fields. Strong magnetic fields are expected to stabilize convective material, but slow rotation reduces meridional circulation and, as a result, reduces mixing, which would prevent atomic diffusion. The physical processes that are active in CP stars, such as pulsation (Dziembowski, Krolikowska & Kosovichev 1988; Soufi, Goupil & Dziembowski 1998) and convective overshooting (Browning, Brun & Toomre 2004; Costa et al. 2019), and their chemical abundances (Turcotte 2002; Murphy 2014), are heavily influenced by rotation.

Renson & Manfroid (2009)'s General Catalogue of Ap and Am stars has 8205 peculiar (or suspected peculiar) stars, making it one of the most comprehensive catalogues of peculiar stars. There are 3652 (candidate) Ap stars, 162 (candidate) HgMn stars, 4299 (candidate) Am stars, and 92 stars that have been incorrectly catalogued as Ap, HgMn, or Am at least once. HD 180347 (= TIC 298969563 = KIC 12253106) is one of the probable Am stars in the General Catalogue of Ap and Am stars by Renson & Manfroid (2009).

Smalley et al. (2011) found HD 180347 to be variable with amplitude less than 0.01 mmag. Later on, Balona et al. (2015) classified the variability as rotational with a period of 4.1 d using data of the nominal *Kepler* mission (Borucki et al. 2010). Recently, Catanzaro et al. (2019) reported HD 180347 among possible pulsators. However, based on the diffusion theory, the He II ionization zone, which excites δ Scuti-type pulsations, should be absent in Am stars. Therefore, it is important to perform a detailed and homogeneous classification and variability study of such a star.

To search for and study the pulsational variabilities in Ap and Am/Fm stars, a dedicated ground-based project the 'Nainital-Cape Survey' was initiated between astronomers of India and South Africa. However, with time, astronomers from other institutions in other countries joined this programme, transforming it into a multi-national collaborative project and a number of results are published (e.g; Ashoka et al. 2000; Martinez et al. 2001; Joshi et al. 2003, 2006, 2009, 2010, 2012, 2016, 2017; Trust et al. 2020, 2021; Joshi et al. 2022). In this paper, we study HD 180347 using data in the *TESS* archive supplemented with high-resolution spectroscopic data from HERMES and spectrophotometric observations available to the public in various databases. The aim of the study is to investigate the photometric variability and fully characterize the candidate Am star HD 180347.

This paper is organized as follows. The spectroscopic observations and data reduction are discussed in Section 2. *TESS* photometry is given in Section 3. Spectral classification is presented in Section 4, while fundamental parameters and individual chemical abundance analyses are given in Section 5 and 6, respectively. Finally, the conclusions are given in Section 7.

2 OBSERVATIONS AND DATA REDUCTION

A high-resolution spectroscopic observation of HD 180347 was done on the night of 2018 November 6, using HERMES (Raskin et al. 2011) mounted at the Cassegrain focus of the 1.2-m Mercator telescope located at La Palma, Spain. This star was observed for a total exposure time of 13.3 min. This spectrograph records optical spectra in the wavelength (λ) range of 377 to 900 nm spanning 55 spectral orders in a single exposure. This instrument has a resolving power of 85 000 in high-resolution mode, with a radial velocity stability of roughly 50 m s^{-1} and an outstanding throughput (Raskin et al. 2011).

The spectrum was reduced using the dedicated HERMES pipeline following the usual reduction procedure for échelle spectra, including subtraction of bias and stray light, flat-field correction, order-by-order extraction, wavelength calibration frames with Thorium–Argon lamps, removal of cosmic rays, and merging of the orders. This procedure resulted in a spectrum with a signal-to-noise ratio (SNR) of 108, 119, and 76 at $\lambda = 500, 650, \text{ and } 810 \text{ nm}$, respectively. The spectrum was manually normalized up to the local continuum using an integrated program ISPEC (Blanco-Cuaresma et al. 2014; Blanco-Cuaresma 2019). Finally, we corrected for barycentric motion in the spectrum. The barycentric Julian date of the observed high-resolution spectrum is BJD 2458429.3586322.

3 TESS DATA PHOTOMETRY

We used the 2-min cadence light curves obtained with *TESS* (Ricker et al. 2015) from 2019 July 18 to August 14 (sector 14), 2019 August 15 to September 10 (sector 15), and 2020 June 9 to July 4 (sector 26) to search for signatures of rotational modulation and/or stellar pulsations. The light curves using pre-search data conditioning (PDC) were selected (PDCSAP.SAP flux column in the FITS file). These are corrected for time-correlated instrumental signatures (Jenkins et al. 2016) and are good enough for our analysis.

The PDC data, as given in the FITS files downloaded from the Barbara A. Mikulski Archive for Space Telescopes (MAST)¹, were used. In constructing the final light curves, the mean flux was subtracted from each individual flux measurement. The result was divided by the mean flux and multiplied by 1087.5 for the conversion to millimagnitudes (mmag). Our classification of variability is based on the General Catalog of Variable Stars (GCVS, Kazarovets et al. 2017).

We calculated the amplitude SNR value for candidate signal peaks in the Fourier transform (Lenz & Breger 2005) to detect significant signal peaks, using a smoothing function across the frequency spectrum to calculate the noise spectrum (Breger et al. 1993). The amplitude of a significant peak exceeds the background noise by a factor of four or more. Simulations, as detailed in Koen (2010), support this significance criterion. Furthermore, Frescura, Engelbrecht & Frank (2008) noted the subjectivity of determining the noise level when calculating the SNR. We augment the SNR approach by calculating the false-alarm probability (FAP) for each peak using the independent frequency method reported in VanderPlas (2018). This criterion calculates the likelihood that a peak was caused by noise rather than an inherent signal. The lower the FAP value, the more likely it is that a given peak is real. A threshold FAP of 10^{-8} (Joshi et al. 2022) was adopted across all the *TESS* data sets. This threshold is also noted by Bowman et al. (2018) to be particularly significant at low frequencies. The detected signals are represented by blue lines in Fig. 1 and their properties are listed in Table 1. The errors listed in this table were determined using a least-square algorithm.

By visual inspection of the Fourier transforms in Fig. 1, only long-period signals (more than 1 d) were detected. For sectors 14 and 26, the frequency values given in Table 1 seem to be consistent with frequencies + harmonic scenario, which suggests spot-induced rotational modulation. In the presence of the harmonic, the rotational frequency is represented by the fundamental. It is possible that the fundamental in some stars is missing or has a very low amplitude, causing the most significant period to be half that of the genuine

¹<https://mast.stsci.edu/portal/Mashup/Clients/Mast/Portal.html>

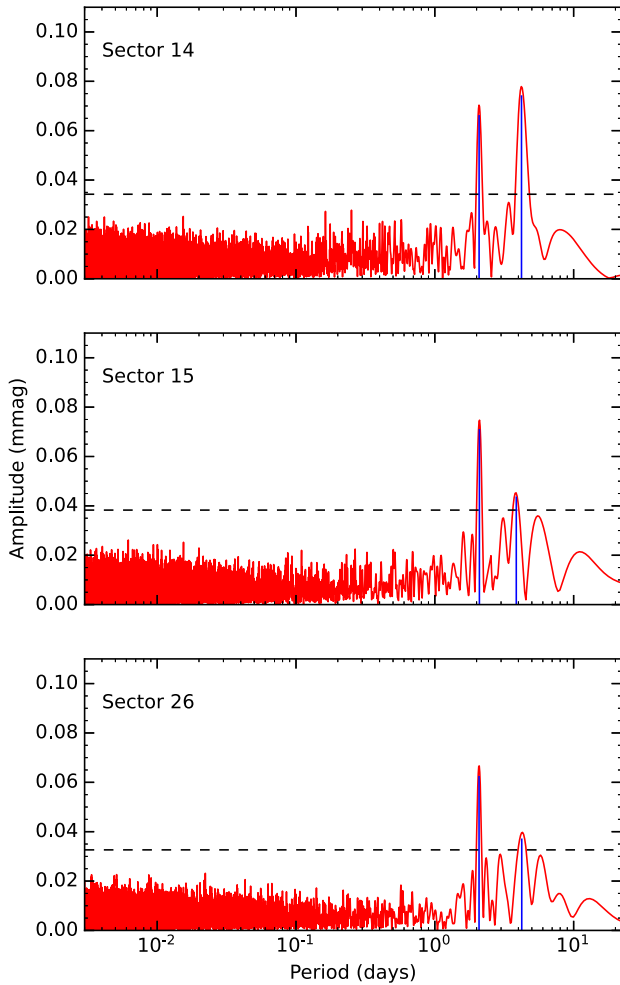


Figure 1. Linear-log periodogram distribution of spectral amplitudes, in mmag, derived from applying the Fourier transform algorithm to the light curves from each sector (given in the top left corner of each panel). The blue lines in the respective panels show the detected signals. The black dashed lines represent the threshold false alarm probability of 10^{-8} , and the peaks above this line are considered significant signals.

rotational period. This could happen in stars with two almost equal-sized diametrically positioned spots (or spotted regions). Based on the Fourier transforms in Fig. 1, HD 180347 could be a typical example of such a case.

Low-level eclipses and rotational signals can be confused. In order to avoid this, the rotational variability identification is limited to stars with amplitudes of less than 10 mmag. To increase the confidence of the variability type of this star, we performed wavelet, autocorrelation functions (ACFs), and composite spectrum analyses of the available *TESS* time series data. These approaches are expected to be more robust to active region evolution than the Fourier transform, which assumes an implicitly steady, sinusoidal signal.

3.1 Wavelet analysis

Star spots could be the cause of the detected signals in the time series data. Star spots, like sunspots, are well known tracers of stellar rotation, but their dynamic behaviour can also be used to study other phenomena like stellar magnetic activity and cycles (García et al. 2010; Mathur et al. 2014). Sunspots change in size and location over time. Sunspots can appear or disappear at any time. If A-type star

spots are comparable to sunspots, one might expect them to behave similarly. Variations in the amplitude of the frequencies are caused by variations in the size and location of starspots. To investigate the frequency change, we created time-frequency diagrams for the *TESS* data sets using the wavelet technique, which allows for a better interpretation of physical features (such as spots) before they are considered for period determination (Torrence & Compo 1998; Mathur et al. 2010).

This technique allows for the analysis of non-stationary signals for a given signal. The reference wavelet was the Morlet wavelet, which is interpreted as the convolution of a sinusoidal and a Gaussian function (Goupillaud, Grossmann & Morlet 1984; Holschneider et al. 1989). The Morlet wavelet has several advantages: (i) it is Gaussian-shaped in the frequency domain, which minimizes ripple effects that can be misinterpreted as oscillations; (ii) the results of Morlet wavelet convolution retain the original signal’s temporal resolution; and (iii) wavelet convolution is computationally efficient.

For each frequency, we calculated the correlation between the mother wavelet and the data. This was accomplished by moving the wavelet along the time axis of the light curves, producing a wavelet power spectrum (WPS). The global wavelets power spectrum (GWPS) was then generated by projecting the WPS along the period axis. Panel (c) of Figs 2, 3, and 4 shows the time-frequency plots of the time series from *TESS* observation sectors 14, 15, and 26, respectively. The blue and black colours in the WPS denote low and high-power regions, respectively. By visual inspection of the GWPS’s shown in panel (d) of Figs 2, 3, and 4, we report rotational periods of 4.10 ± 0.44 , 3.54 ± 0.45 , and 4.10 ± 0.45 , respectively. Within error limits, these results are consistent with those obtained directly from Fourier transforms in Fig. 1.

3.2 Autocorrelation functions

The ACFs show how similar light curves are to themselves at certain time differences (McQuillan, Aigrain & Mazeh 2013; McQuillan, Mazeh & Aigrain 2014). Briefly, the autocorrelation function (ACF) is given by:

$$ACF_{\tau} = \frac{1}{N} \frac{\sum_{i=1}^N (x(t_i) - \bar{x})(x(t_i - \tau) - \bar{x})}{\sigma^2}, \quad (1)$$

where τ is the lag time shift between the same time-series, $x(t_i)$ is the time-series value at time t_i , \bar{x} is the temporal mean of the time series, and σ^2 is the time-series variance. The variance is given by:

$$\sigma^2 = \frac{\sum_{i=1}^N (x(t_i) - \bar{x})^2}{N}. \quad (2)$$

At time lag shift between the time series, $\tau = 0$, the ACF in equation 1 reduces to:

$$ACF_{\tau=0} = \frac{1}{N} \frac{\sum_{i=1}^N (x(t_i) - \bar{x})^2}{\sigma^2}. \quad (3)$$

A comparison of equations (2) and (3) results in $ACF_{\tau=0} = 1$. When a time series contains a dominant repeated signal of the period (P_{ACF}), probably created by the presence of spots, the pattern is expected to anticorrelate and correlate such that $ACF_{\tau=kP_{ACF}/2} = -1$ and $ACF_{\tau=kP_{ACF}} = 1$, respectively, where $k = 1, 2, 3, 4, \dots, m$ and $mP_{ACF} < t_N$. However, this is not the case when the whole time-series is correlated with itself due to limited overlap, for any time-lag not equal to zero. The ACF oscillates between maximum and minimum values as the patterns become correlated and anticorrelated, and the amplitude decreases as the overlap decreases. The overall amplitude of ACFs can additionally be reduced due to variations of signals in

Table 1. Properties of signals detected in the *TESS* data obtained in three different sectors 14, 15, and 26. Listed is the frequency, period, amplitude, phase, probability of false alarm ($\log_{10}(\text{FAP})$), and signal-to-noise ratio (SNR) as determined from the Fourier transforms.

<i>TESS</i> Observation Sector	Frequency (d^{-1})	Period (d)	Amplitude (mmag)	Phase (rad)	$\log_{10}(\text{FAP})$	SNR
14	0.2375 ± 0.0015	4.211 ± 0.027	0.079 ± 0.006	-1.72 ± 0.07	-37	21
	0.4798 ± 0.0016	2.084 ± 0.007	0.077 ± 0.006	1.41 ± 0.08	-32	19
15	0.4775 ± 0.0018	2.094 ± 0.008	0.074 ± 0.006	-0.80 ± 0.08	-33	19
	0.2589 ± 0.0031	3.862 ± 0.046	0.043 ± 0.006	1.85 ± 0.13	-9	12
26	0.4803 ± 0.0017	2.082 ± 0.007	0.062 ± 0.005	-2.69 ± 0.08	-32	19
	0.2365 ± 0.0029	4.228 ± 0.052	0.042 ± 0.005	2.49 ± 0.12	-9	12

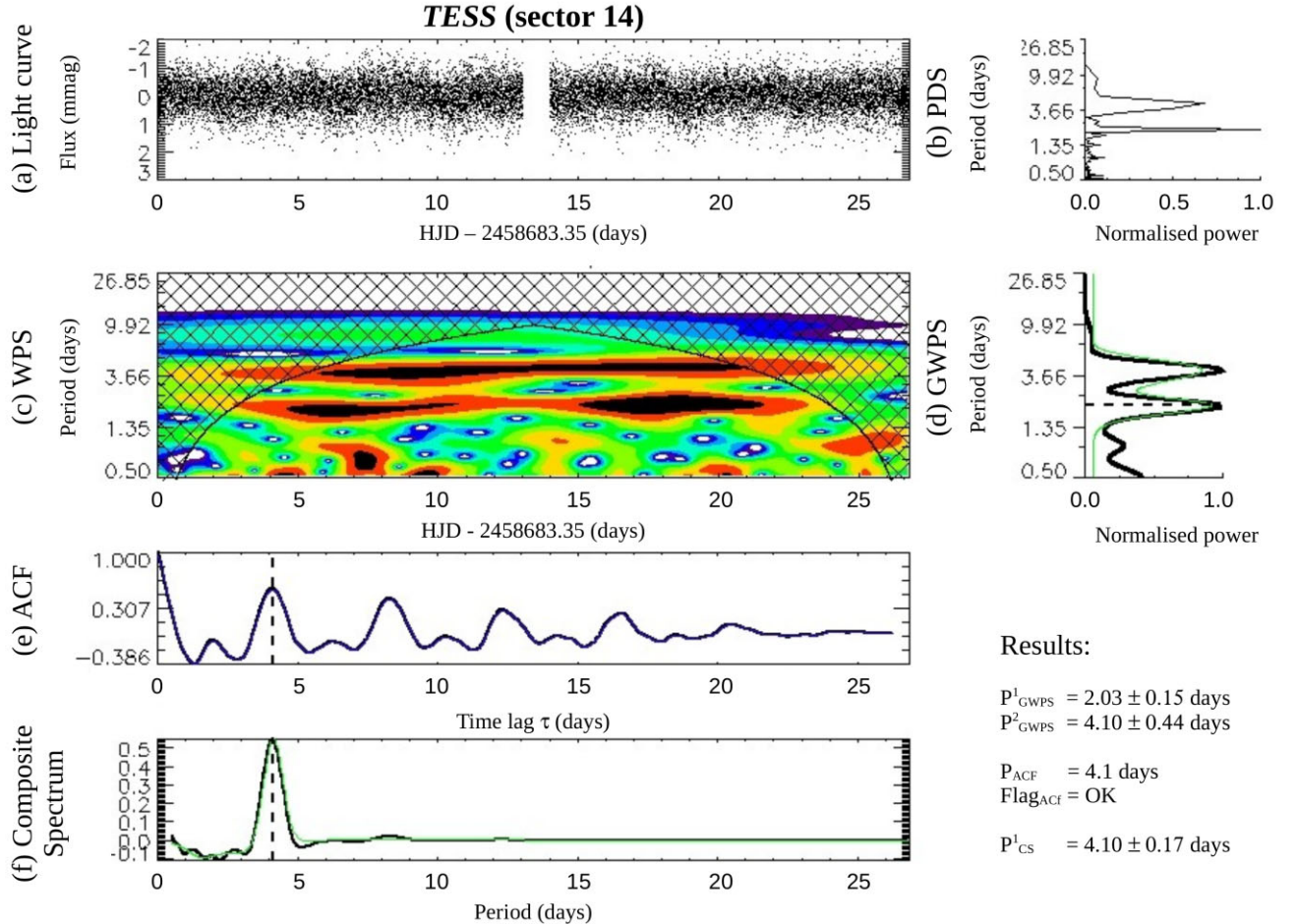


Figure 2. Search for the rotation period of HD 180347 based on the *TESS* data from sector 14. Panel (a) shows the light curve while the power density spectrum (PDS) as a function of the period between 0.5 and 27 d is given in panel (b). The wavelet power spectrum (WPS) computed using a Morlet wavelet between 0.5 and 27 d on a logarithmic scale is shown in panel (c) and the associated global wavelet power spectrum (GWPS) is given in panel (d). The colours black and blue represent high and low power, respectively. The autocorrelation function (ACF) of the full light curve and the composite spectrum (CS) (Ceillier et al. 2016; Ceillier et al. 2017), plotted between 0 and 27 d, are presented in panels (e) and (f), respectively. The cone of influence corresponding to the unreliable results is represented by the black-crossed area in the WPS. The automatically detected rotational period estimates are denoted by the black dashed lines. A summary of the results is given in the bottom right corner. The quality flag Flag_{ACF} indicates whether the selected P_{ACF} corresponds to the dominant of the regularly spaced peaks of the ACF.

the time series, which could be the reflection of variations in the size of the spot (active region). Therefore, at time lags greater than zero, the ACF resembles a displacement of an underdamped simple harmonic oscillator (uSHO) (Giles, Collier Cameron & Haywood 2017):

$$y(\tau) = e^{-\tau/\tau_{\text{DT}}} \left(A \cos \left(\frac{2\pi\tau}{P_{\text{ACF}}} \right) + B \cos \left(\frac{4\pi\tau}{P_{\text{ACF}}} \right) + y_0 \right), \quad (4)$$

where

$$\tau = \Delta T \times n,$$

ΔT is the median time difference of the light-curve, n ascends from 0 to the total number of ACFs, $y(\tau)$ is the ACF, τ_{DT} is the decay-time scale of the ACF, P_{ACF} is the time lag corresponding to the first maximum of the ACF that represents the rotation period of the star,

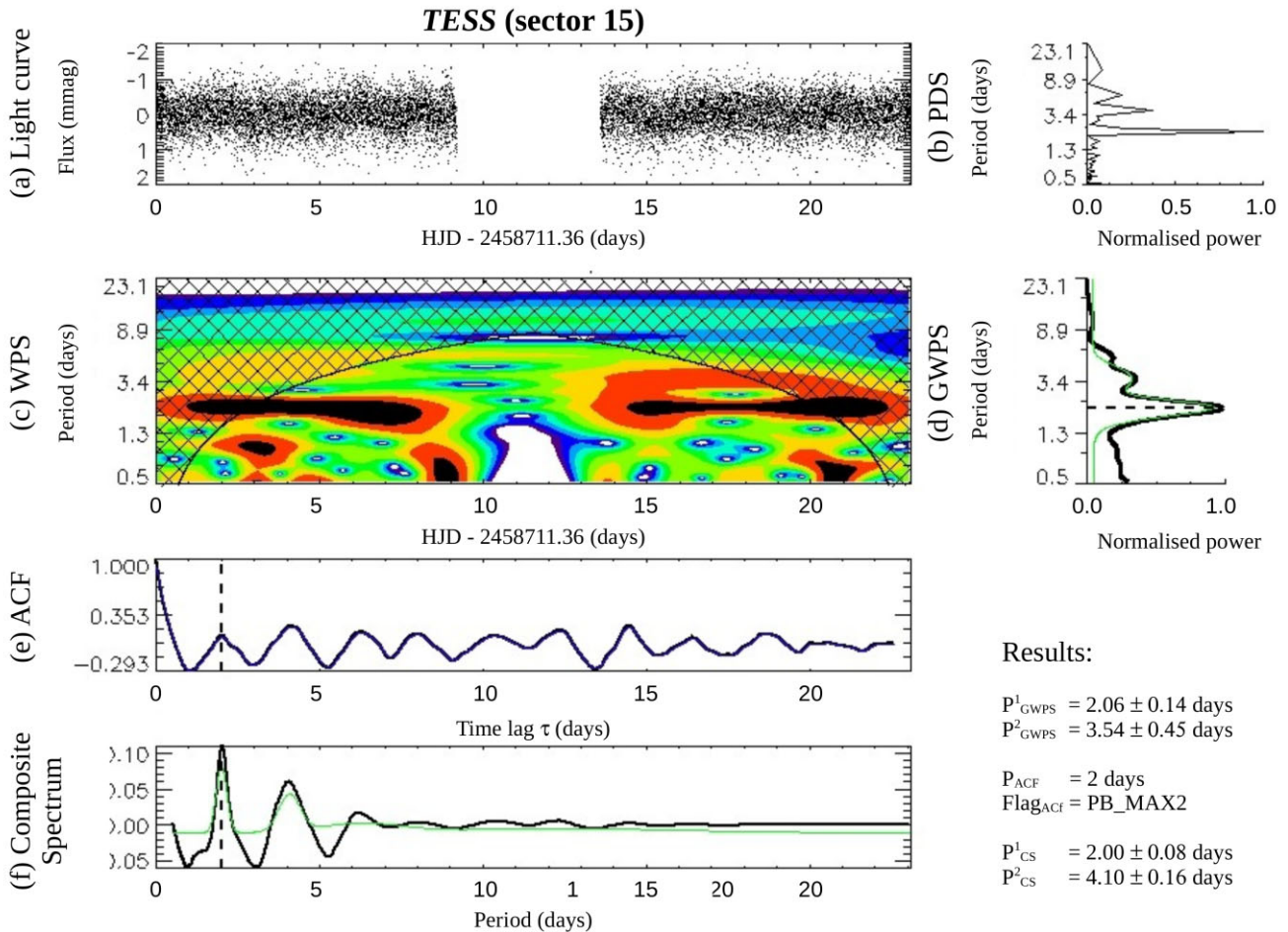


Figure 3. Same as Fig. 2 but for the *TESS* data from sector 15.

and A , B , and y_0 that do not represent any physical stellar properties but are constants that are needed in the fit of an uSHO.

Using equation (1), we calculated ACFs of the time-series at different time-lags as represented in panel (e) of Figs 2, 3, and 4. The first dominant peak in the ACF was selected as the P_{ACF} . The obtained values of P_{ACF} are 4.1, 2, and 1.98 d, for sectors 14, 15, and 26, respectively. In panel (e) of Fig. 2, the ACF shows subpeaks at $\tau = kP_{\text{ACF}}/2$. The subpeaks in panel (e) of Figs 3 and 4 are of comparable strength to the major peaks. The strength of the subpeaks increases due to the dominance of secondary signals (perhaps harmonics) as shown in panels (b), (c), and (d) of Figs 3 and 4. This is thought to occur when slightly weaker spotted regions are diametrically opposite to the dominant spotted region as earlier mentioned in Section 3. This means that the obtained P_{ACF} values for sectors 15 and 26 are half the genuine values.

3.3 Composite spectrum

The ACF and the GWPS are sensitive to different issues in the light curve. When we combine the two, we can find periods that are intrinsic to the star. The composite spectrum (CS) combines the two preceding methods (wavelet and ACF) (Ceillier et al. 2016; Ceillier et al. 2017).

We used an exponentially decreasing function to fit the smoothed ACF. To obtain the normalized ACF, the fit was subtracted from the smoothed ACF. We calculated the CS by multiplying the normalized

ACF and GWPS. This increases the height of the peaks in both curves while decreasing the height of the peaks in one of the two. The CS is very sensitive to the periods detected in both ACF and GWPS, which makes it reliable up to about 95 per cent of the time (Aigrain et al. 2015).

We calculated the period, P_{CS} , by fitting the peaks in the CS with Gaussian functions. The central period of the function corresponding to the highest peak was taken as the P_{CS} . The associated uncertainty corresponds to the peak's half width at half-maximum (HWHM). By visual inspection of panel (f) of Figs 2, 3, and 4, we report rotational periods of 4.10 ± 0.17 , 4.10 ± 0.16 , and 4.10 ± 0.15 d, respectively. The only difference among the P_{CS} values is the uncertainty.

The results of *TESS* photometry investigations show no evidence of pulsational variability, as previously proposed by Catanzaro et al. (2019). Following the criterion by McQuillan et al. (2013), Ceillier et al. (2016), and Ceillier et al. (2017), the observed signals are rotational. Based on the strengths of the methods (Ceillier et al. 2017), we take P_{CS} as the ultimate rotational period for HD 180347. The amplitude of the rotational signal indicates the spot size, which gives a clue about the magnetic field's strength. The rotational signal amplitudes range from 0.07 to 0.08 mmag, which is much larger than the average amplitude (0.02 mmag) of A and Am stars with 'hump and spike' features in their Fourier transforms investigated by Trust et al. (2020). This means that HD 180347 has spots that are about four times larger and so have greater magnetic fields. Magnetic fields are vital in stabilizing the material, which allows for atomic diffusion. A

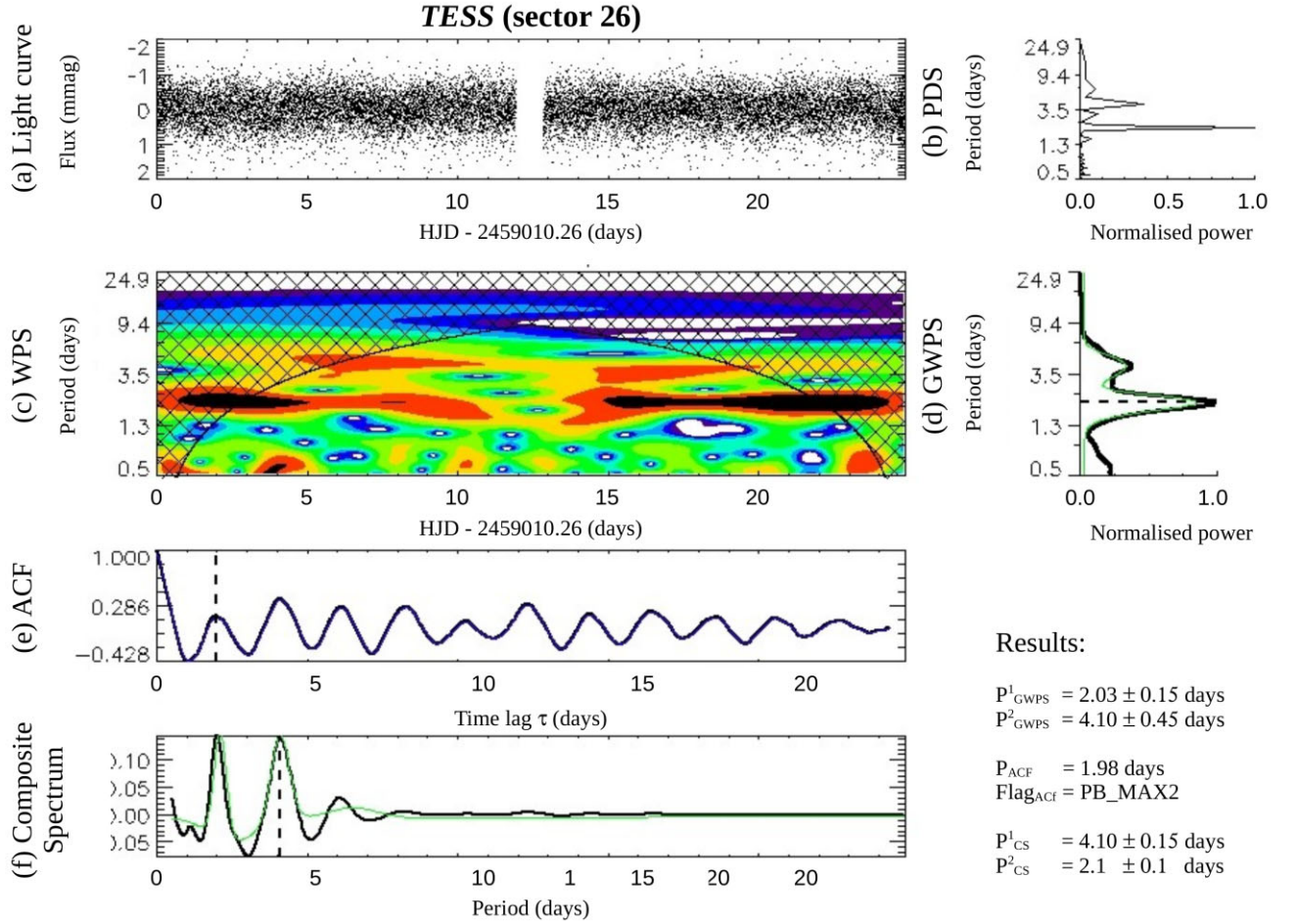


Figure 4. Same as Fig. 2 but for the *TESS* data from sector 26.

spectropolarimetric analysis of this star is required to determine the strength of its magnetic field. This, however, is beyond the scope of this research.

4 SPECTRAL CLASSIFICATION

We used the MK classification system (Morgan, Keenan & Kellman 1943; Gray & Corbally 2009) to perform a spectral classification analysis on HD 180347. It can be used to determine the chemical peculiarity of a star (Gray & Corbally 2009). The spectral type and luminosity class are determined by comparing the observed spectra to well known standards while accounting for crucial hydrogen and metal lines. We used the high-resolution HERMES spectrum to do the spectral classification of HD 180347.

The HERMES spectrum of HD 180347 was classified with the help of the code MKCLASS² (Gray & Corbally 2014) in combination with the standard libraries given by Gray et al. (2003). The spectra of this library were obtained with the 0.8-m telescope of the Dark Sky Observatory (DSO) in the north-west of North Carolina (USA) by using the Gray/Miller classification spectrograph with a grating having either 600 or 1200 grooves mm^{-1} . The standard spectra span the violet-green wavelength region at a resolution range of 0.18–0.36 nm/2 pixels (Gray & Corbally 2014).

Our HERMES spectrum is not observed with the same spectrograph/grating combination as the spectra of the standard library. We, therefore, truncated its wavelength region, re-binned it, and convoluted the spectrum with a Gaussian of appropriate full width at half-maximum of 0.16 nm to match the specifications of the standards as closely as possible.

MKCLASS uses the metric-distance technique (LaSala 1994), which is based on a weighted least-square comparison of the program spectrum with that of the MK standard stars (Gray & Corbally 2014), to determine the spectral type based on (i) hydrogen lines ($\text{H}\gamma$ and $\text{H}\sigma$), (ii) metal lines, and (iii) the Ca II K-line. For a chemically normal star, this should lead to the same results while different spectral types in these three regions are expected in the case of a chemically peculiar star (Gray & Corbally 2009). With this method, we found a spectral type of kA1hA8mA8, confirming the classification of HD 180347 as an Am star, first reported by Bidelman (1985).

5 FUNDAMENTAL STELLAR PARAMETERS

High-resolution spectroscopy is a robust method to derive accurate values of the basic stellar parameters like the effective temperature (T_{eff}), surface gravity ($\log g$), and metallicity ($[\text{M}/\text{H}]$) (Section 5.1). Once they are known, they can be used to calculate values of additional fundamental stellar parameters (Section 5.2).

²<http://www.appstate.edu/~grayro/mkclass/>

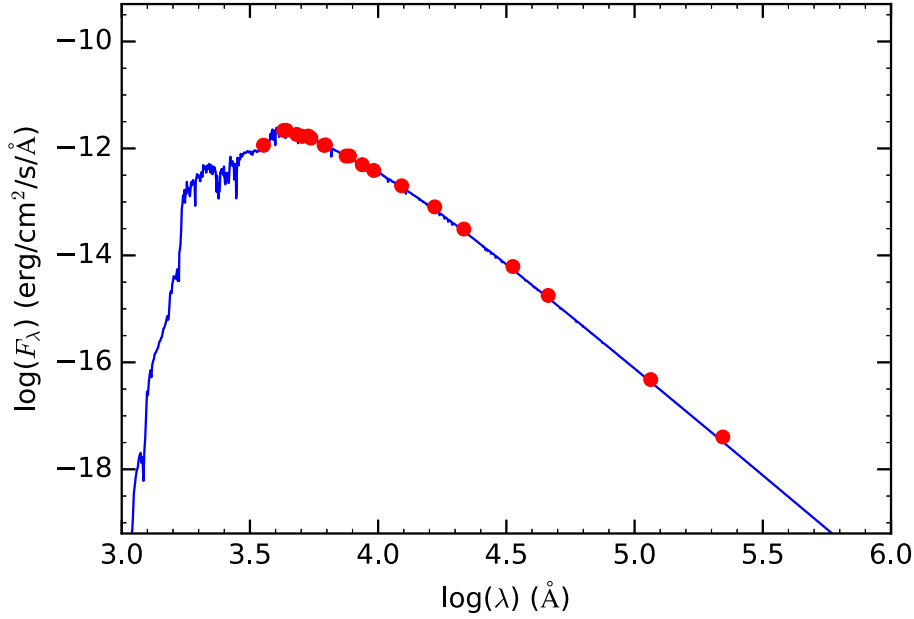


Figure 5. The red-filled circles represent the SED of HD 180347. The blue solid line represents the best fit to the data obtained using the VOSA tool.

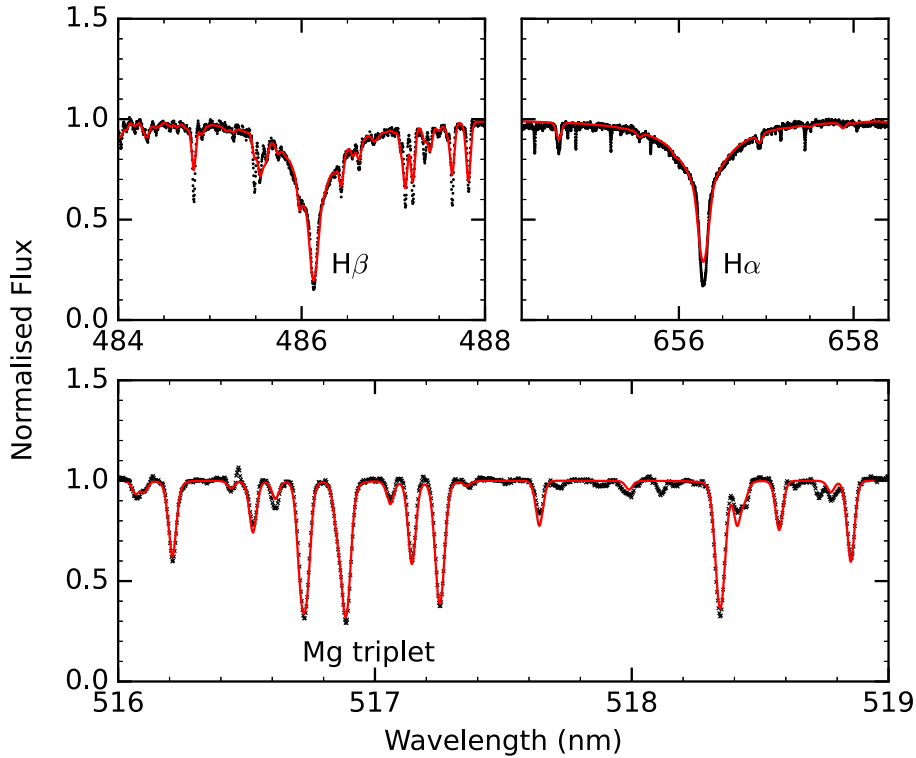


Figure 6. The $H\beta$ (top left), Mg I triplet (bottom), and $H\alpha$ (top right) line regions for the target star. The observed (black) and synthetic spectra (red) are shown. The synthetic spectrum was obtained with LTE consideration. The majority of the narrow features in the observed spectrum that the models do not fit are telluric lines.

5.1 Derived stellar parameters

To achieve convergence during synthesis, knowledge of a good initial guess for the basic stellar parameters is critical. Therefore, we derived T_{eff} , $\log g$, and $[M/H]$ in two steps.

In the first step, the spectral energy distribution (SED) of HD 180347 was used to obtain preliminary values for T_{eff} , $\log g$,

and $[M/H]$ (cf. Trust et al. 2021). Using the VOSA³ (Bayo et al. 2008) tool and the ATLAS9 Kurucz ODFNEW/NOVER models (Castelli & Kurucz 2003), we performed a least-square fit to the SED

³<http://svo2.cab.inta-csic.es/theory/vosa/>

Table 2. Overview of the values of fundamental parameters of HD 180347 resulting from this study and those available in the literature. The top part lists the parameters directly obtained from the HERMES spectrum, while the bottom part gives those derived from them. Within the error limits, the literature values that disagree with our results are provided in italics.

Parameter	Value	Error	Reference
T_{eff} (K)	7740	170	This study
	7685	–	McDonald, Zijlstra & Boyer (2012)
	7900	140	Catanzaro et al. (2015)
	7709	264	Mathur et al. (2017)
	7522	97	Andrae et al. (2018)
	7699	269	Murphy et al. (2019)
	7600	125	Catanzaro et al. (2019)
$\log g$ (cm s^{-2})	7544	97	Andrae et al. (2022)
	3.98	0.12	This study
	3.85	0.07	Catanzaro et al. (2015)
	3.99	0.19	Mathur et al. (2017)
	4.11	0.09	Murphy et al. (2019)
	4.0	0.25	Catanzaro et al. (2019)
	4.13	–	Andrae et al. (2022)
[M/H] (dex)	0.11	0.08	This study
ξ (km s^{-1})	3.81	0.12	This study
	4.7	0.4	Catanzaro et al. (2015)
$\nu \sin i$ (km s^{-1})	14	2	This study
	12	1	Catanzaro et al. (2015)
	11	1	Catanzaro et al. (2019)
	14.64	–	Jönsson et al. (2020)
v_{rad} (km s^{-1})	9.3	0.3	This study
	5.1	0.1	Catanzaro et al. (2019)
	9.30	0.01	Jönsson et al. (2020)
	5.2	1	Blomme et al. (2022)
$\log(L_{\star}/L_{\odot})$	0.993	0.030	This study
	0.97	–	Andrae et al. (2018)
	0.88	–	Catanzaro et al. (2019)
R_{\star} (R_{\odot})	1.75	0.14	This study
	2.19	0.56	Mathur et al. (2017)
	1.80	0.05	Andrae et al. (2018)
	1.83	0.14	Murphy et al. (2019)
v_{eq} (km s^{-1})	22	1	This study
i ($^{\circ}$)	40	5	This study
M_{\star} (M_{\odot})	1.740	0.023	This study
	1.71	0.26	Mathur et al. (2017)
	1.58	0.25	Murphy et al. (2019)
age (Gyr)	0.85	0.18	This study
	0.14–1.1	–	Catanzaro et al. (2019)

to obtain T_{eff} , $\log g$, and [M/H] as 7750 ± 250 K, 4.0 ± 0.5 cm s^{-2} , and 0.5 ± 0.30 dex, respectively. The uncertainties in the parameters are the propagated uncertainties in the fit parameter calculation. We emphasize that these SED results only served the purpose of being first guesses for spectroscopic analysis. The best model is represented by a blue line in Fig. 5.

In the second step, the HERMES spectrum was used to derive the radial velocity (v_{rad} ; Section 5.1.1), $\nu \sin i$ (Section 5.1.2), and the microturbulent velocity (ξ) and final values of T_{eff} , $\log g$, and [M/H] (Section 5.1.3).

5.1.1 Radial velocity

We calculated the radial velocity v_{rad} by computing the cross-correlation function (CCF) with various pre-selected masks created

from line lists using the code iSPEC⁴. We found a v_{rad} value of 9.3 ± 0.3 km s^{-1} corresponding to the time that the HERMES spectrum was observed (BJD 2458429.3586322).

5.1.2 Projected rotational velocity

Using the initial values from the SED analysis, $\nu \sin i$ was calculated by comparing the observed spectrum to a grid of synthetic spectra. The least-square method was used in this comparison, which was based on the MINUIT minimization software, which is included in the GIRFIT package (Frémat et al. 2006). We interpolated the spectrum in a grid of stellar fluxes computed using plane-parallel ATLAS9⁵ model atmospheres (Castelli & Kurucz 2003) for T_{eff} , $\log g$, and v_{rad} values of 7750 K, 4.0 cm s^{-2} , and 9.3 km s^{-1} , respectively, and varied $\nu \sin i$ values in the range 0–100 km s^{-1} with steps of 1 km s^{-1} .

Based on the initial prediction of T_{eff} (7750 K) from SED, we chose the Mg I triplet region (516–519 nm) for $\nu \sin i$ determination. In addition to other metal lines, stars with T_{eff} less than 9000 K, Mg I triplet is sensitive to the $\nu \sin i$ (cf. Catanzaro et al. 2015, 2019; Trust et al. 2021). In this spectral region, Mg I triplet lines predominate; nevertheless, additional metal lines such as iron (516.227, 516.541, 516.628, 517.16 nm), nickel (517.656 nm), and titanium (518.59, 518.869 nm) are also present. With this method, the resulting value for $\nu \sin i$ is 14 ± 2 km s^{-1} .

5.1.3 Effective temperature, surface gravity, metallicity, and microturbulent velocity

We determined T_{eff} , $\log g$, [M/H], and ξ by synthesizing stellar spectra with the MOOG radiative transfer code⁶ (Snedden et al. 2012). We used the ATLAS9 model atmospheres, the Vienna Atomic Line Database (VALD) line list (Kupka et al. 1999), and the solar abundances of Asplund et al. (2009), all of which were combined in the integrated software package iSPEC. The Balmer lines are T_{eff} sensitive but lose $\log g$ sensitivity for stars with T_{eff} less than 8000 K. T_{eff} and $\log g$ were estimated from the hydrogen line profiles and Fe I/Fe II lines, respectively. [M/H] was determined from all available lines, with Fe, Ca, and Ti lines dominating. Since $\nu \sin i$ is low, the ξ was determined by fitting Fe and Ti II lines and its initial guess was calculated from the relation (Gebran et al. 2014),

$$\xi = 3.31 \times \exp \left[- \left(\log \left(\frac{T_{\text{eff}}}{8071.03} \right)^2 / 0.01045 \right) \right]. \quad (5)$$

The resulting values are 7740 ± 170 K for T_{eff} , 3.98 ± 0.12 cm s^{-2} for $\log g$, 0.11 ± 0.08 dex for [M/H], and 3.81 ± 0.12 km s^{-1} for ξ . Uncertainties in parameters were calculated as the change in parameter values that raises χ^2 by one (Lampton, Margon & Bowyer 1976).

Fig. 6 shows the H β (top left), Mg I triplet (bottom), and H α (top right) line regions for the HERMES spectrum of HD 180347 (black) and the synthetic (red) spectra computed with the final values of the atmospheric parameters as listed in the top part of Table 2. Our results, within the error bounds, accord with some of those from prior studies, as indicated in Table 2. The literature values that differ from our results are shown in italics in this table.

⁴<https://www.blancocuaresma.com/s/iSpec>

⁵http://www.stsci.edu/hst/observatory/crds/castelli_kurucz_atlas.html

⁶<https://www.as.utexas.edu/chris/moog.html>

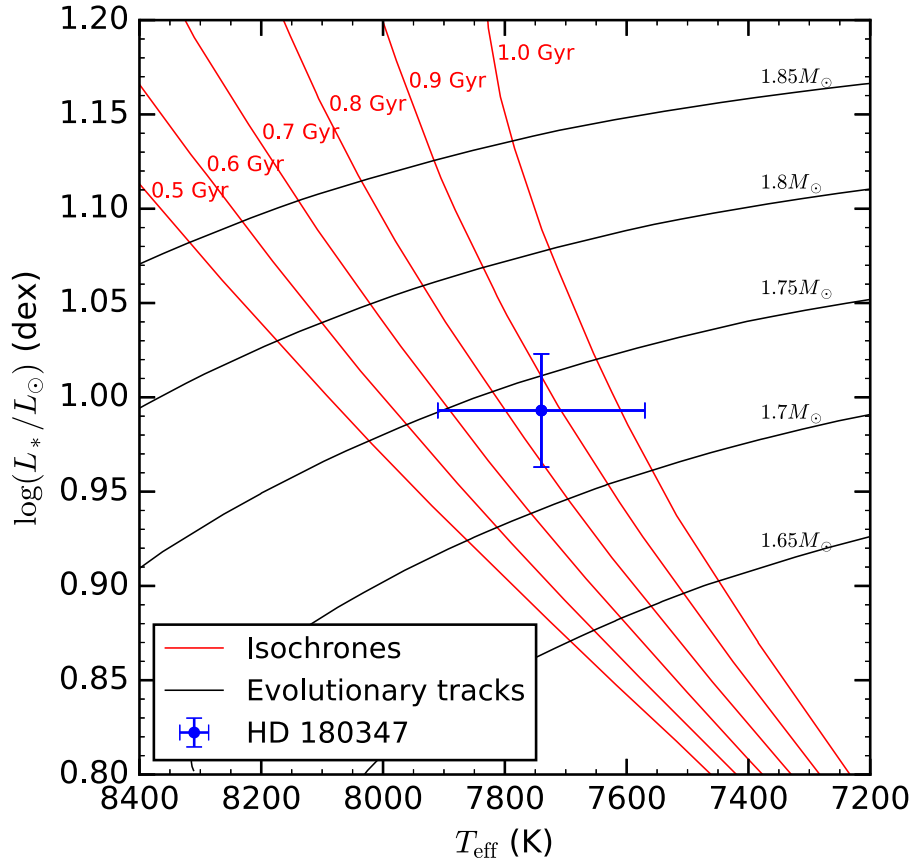


Figure 7. The HR diagram showing the position of HD 180347 relative to a number of the PARSEC 1.2 evolutionary tracks (*black solid lines*) and isochrones (*red solid lines*) (Bressan et al. 2012).

5.2 Calculated stellar parameters

5.2.1 Luminosity and radius

Based on the standard technique, we determined the luminosity ($\log(L_*/L_\odot)$) (cf. Trust et al. 2021). We determined the reddening parameter $E(B - V)$ from 3D models (Green 2018; Green et al. 2019) using the GAIA parallaxes (Evans et al. 2018) and the stellar galactic coordinates from the SIMBAD data base⁷ (Wenger et al. 2000) and found a value of 0.0173 ± 0.0015 mag. Using the temperature-dependent function by Flower (1996) revised by Torres (2010), the bolometric correction (BC) was calculated. We computed the absolute magnitude (M_v) using GAIA parallaxes (Evans et al. 2018). Uncertainties in V -band indices, parallax, and T_{eff} contribute to the uncertainties in $\log(L_*/L_\odot)$. We used the method described in Trust et al. (2021) to calculate the stellar radius (R_*) from the Stefan–Boltzmann law (Boltzmann 1884; Paul et al. 2015; Montambaux 2018). The procedure produced a M_v value of 2.252 ± 0.083 mag, a BC value of 0.0283 ± 0.0055 mag, a $\log(L_*/L_\odot)$ value of 0.993 ± 0.030 , and a R_* value of $1.75 \pm 0.14 R_\odot$. Within the error limits, our results are in agreement with those reported in Andrae et al. (2018) as shown in Table 2.

5.2.2 Equatorial rotational velocity and inclination angle

Using the rotational period (4.10 ± 0.17 d) obtained from the TESS data and the value of R_* , the equatorial rotational velocity v_{eq} was calculated (cf. Trust et al. 2020). We constrained the inclination angle (i) from the relationship between $v \sin i$ and the equatorial rotational velocity (v_{eq}). We report the values of v_{eq} and i to be 22 ± 1 km s⁻¹ and $40 \pm 5^\circ$, respectively.

5.2.3 Stellar mass and age

Using the T_{eff} and $\log(L_*/L_\odot)$ values derived in the previous sections, the stellar mass (M_*) and age were determined by interpolating the PARSEC 1.2 evolutionary tracks and isochrones (Bressan et al. 2012), respectively. The grids of evolutionary tracks span a mass range of 1.5–2.5 M_\odot while the isochrones have ages ranging between 0.2 and 1 Gyr. The results for M_* and age are $1.740 \pm 0.023 M_\odot$ and 0.85 ± 0.18 Gyr, respectively. Fig. 7 represents a Hertzsprung–Russell (HR) diagram showing the position of HD 180347 relative to a number of the PARSEC 1.2 evolutionary tracks and isochrones. The values of the fundamental parameters derived in this section are listed in the bottom part of Table 2.

6 INDIVIDUAL CHEMICAL ABUNDANCES

With a high-resolution HERMES spectrum with an SNR ~ 100 at hand, it is possible to derive the abundances of chemical elements with a sufficient number of detectable absorption lines in the observed

⁷<https://simbad.u-strasbg.fr/simbad/>

Table 3. Results of the abundance analysis of HD 180347 based on the observed HERMES spectrum and with LTE consideration. Listed in column 2 are the individual chemical abundances inferred for our target star and column 3 gives the solar abundances (Asplund et al. 2009). The number of spectral lines from which the abundances were derived is given between brackets.

Element	$\log(N_{\text{el}}/N_{\text{Tot}})_*$	$\log(N_{\text{el}}/N_{\text{Tot}})_{\odot}$
C	-4.26 ± 0.16 (7)	-3.61
O	-3.87 ± 0.11 (3)	-3.35
Na	-5.19 ± 0.20 (6)	-5.80
Mg	-4.63 ± 0.17 (14)	-4.44
Si	-4.24 ± 0.16 (43)	-4.53
S	-4.63 ± 0.13 (22)	-4.92
K	-7.14 ± 0.12 (1)	-7.01
Ca	-6.62 ± 0.20 (28)	-5.70
Sc	-10.42 ± 0.11 (4)	-8.89
Ti	-7.07 ± 0.16 (102)	-7.09
V	-7.50 ± 0.12 (36)	-8.11
Cr	-6.01 ± 0.15 (127)	-6.40
Mn	-6.40 ± 0.09 (57)	-6.61
Fe	-4.33 ± 0.09 (368)	-4.54
Co	-6.42 ± 0.12 (20)	-7.05
Ni	-5.28 ± 0.10 (121)	-5.82
Cu	-7.01 ± 0.17 (7)	-7.85
Zn	-6.98 ± 0.13 (2)	-7.48
Sr	-8.23 ± 0.15 (4)	-9.17
Y	-9.03 ± 0.14 (29)	-9.83
Zr	-8.87 ± 0.09 (4)	-9.51
Ba	-8.49 ± 0.10 (4)	-9.85
La	-9.54 ± 0.20 (28)	-10.94
Ce	-9.13 ± 0.12 (32)	-10.46
Nd	-9.51 ± 0.11 (18)	-10.62

spectrum. We started with an abundance analysis for all the elements assuming local thermodynamic equilibrium (LTE; Section 6.1). Afterwards, for 13 elements, we investigated the effects of the non-local thermodynamic equilibrium (NLTE) line formation on their derived abundances (Section 6.2).

6.1 LTE abundance analysis

The individual chemical abundances were calculated via direct fitting of theoretical profiles of individual spectral lines using the $\nu \sin i$ and v_{rad} values derived in Section 5.1. We used the SYNTHV_NLTE code (Tsymbal, Ryabchikova & Sitnova 2019) in combination with a grid of pre-computed atmospheric models from the LLmodels package (Shulyak et al. 2004). The calculations were carried out using the IDL visualization program BINMAG6⁸ (Kochukhov 2018). LTE was assumed during spectrum synthesis. The line lists and atomic parameters were extracted from the 3D release of the Vienna Atomic Line Database (VALD3; Ryabchikova et al. 2015).

We used a χ^2 minimization of the difference between the observed and synthetic spectra to derive the abundances for each individual line present in the wavelength interval. Table 3 shows the average individual chemical abundances and their uncertainties expressed as $\log(N_{\text{el}}/N_{\text{Tot}})$. The abundance pattern, in relation to solar abundances (Asplund et al. 2009), is shown in Fig. 8. The uncertainties in abundances result from a combined dependence of the errors on T_{eff} , $\log g$, $\nu \sin i$, ξ , the position of the continuum of the normalized HERMES spectrum, and the accuracy of the oscillator strengths

($\log(gf)$) of the lines considered in our analysis. We should be cautious about the abundances of elements whose lines are present in less than three spectral lines because they were calculated from a small number of lines.

Calcium and scandium are found to be underabundant relative to the solar abundances, by ≈ 0.92 and ≈ 1.53 dex, respectively, while the heavy elements, such as strontium, yttrium, zirconium, barium, lanthanum, cerium, and neodymium are overabundant. Our abundance analysis reveals a chemical pattern typical for Am stars. As shown in Fig. 9, our LTE abundances are in agreement with those determined by Catanzaro et al. (2015) and Catanzaro et al. (2019) in their LTE analyses.

6.2 NLTE abundance analysis

We determined the NLTE abundances for carbon, oxygen, sodium, magnesium, silicon, potassium, calcium, scandium, titanium, zinc, strontium, zirconium, and barium. These elements are some of the most easily observed elements in A-type stars. Carbon, oxygen, magnesium, silicon, and calcium are examples of α -elements. An accurate determination of their abundances is critical for a better understanding of the history of α -process nucleosynthesis in the universe, the formation and evolution of a large number of galaxies, as well as the physics of stars and planetary systems. The α -process is a type of nuclear fusion in which helium is converted into heavier elements in a star (Narlikar 1995). Moreover, having the best possible abundances of calcium, scandium, strontium, zirconium, and barium is also important for the correct classification of chemically peculiar stars (Preston 1974).

We used the code DETAIL (Giddings 1981; Butler 1984) based on the accelerated Λ -iteration method (Rybicki & Hummer 1991, 1992) to solve the radiative transfer and statistical equilibrium equations. The DETAIL opacity package was updated by Przybilla, Nieva & Butler (2011). The model atoms were produced and described in detail by Sitnova, Mashonkina & Ryabchikova (2013, O I), Alexeeva, Pakhomov & Mashonkina (2014, Na I), Alexeeva et al. (2018, Mg I–II), Mashonkina (2020, Si I–II), Neretina et al. (2020, K I), Mashonkina, Korn & Przybilla (2007, Ca I–II), Mashonkina & Romanovskaya (2022, Sc II), and Mashonkina et al. (2020, Sr II, Zr II–Zr III, Ba II). We denote the statistical equilibrium and thermal (Saha–Boltzmann) number densities as n_{NLTE} and n_{LTE} , respectively. The obtained departure coefficients ($b = n_{\text{NLTE}}/n_{\text{LTE}}$) were then used to calculate the synthetic NLTE spectrum with the code SYNTHV_NLTE (Tsymbal et al. 2019). Using the visualization tool BinMag6 (Kochukhov 2018), we compared the synthetic NLTE and observed spectra and performed spectral line fitting. For consistency with the LTE calculations discussed in Section 6.1, we used the same model atmosphere and the line list. Fig. 10 shows the best NLTE fits to the selected observed lines and, for comparison, the LTE profiles computed using the abundances obtained from the NLTE analysis.

For lines of C I–II, Ti I–II, and Zn I, we applied the NLTE abundance corrections predicted by Alexeeva, Ryabchikova & Mashonkina (2016), Sitnova, Mashonkina & Ryabchikova (2016), and Sitnova et al. (2022), respectively.

We cannot perform the NLTE calculations for the Fe-group elements V to Ni due to the absence of the model atoms, and, for the atmospheric parameter range with which we are concerned, there are no predicted NLTE abundance corrections in the literature. Having inspected the NLTE and LTE abundances published by Mashonkina et al. (2020) for lines of Fe I and Fe II in two A-type dwarf stars with $T_{\text{eff}} = 7250$ and 9380 K, we expect minor NLTE effects on

⁸<https://www.astro.uu.se/oleg/binmag.html>

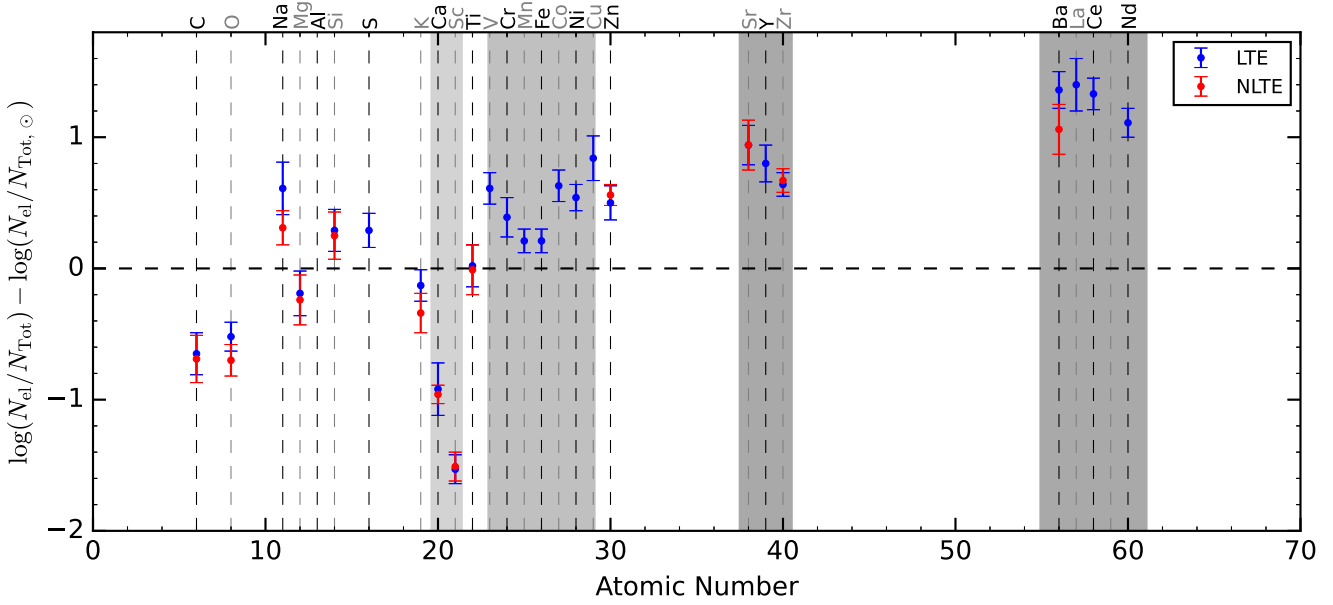


Figure 8. The individual chemical abundance pattern for HD 180347. The horizontal dashed line indicates solar abundances (Asplund et al. 2009). The light elements (Ca and Sc) and heavy elements (Fe, Co, Ni, Cu, Sr, Y, Zr, Ba, La, Ce, Pr, and Nd), important for the classification of Am stars, are highlighted with a gray background. The *blue* and *red* symbols represent the LTE and NLTE abundances, respectively.

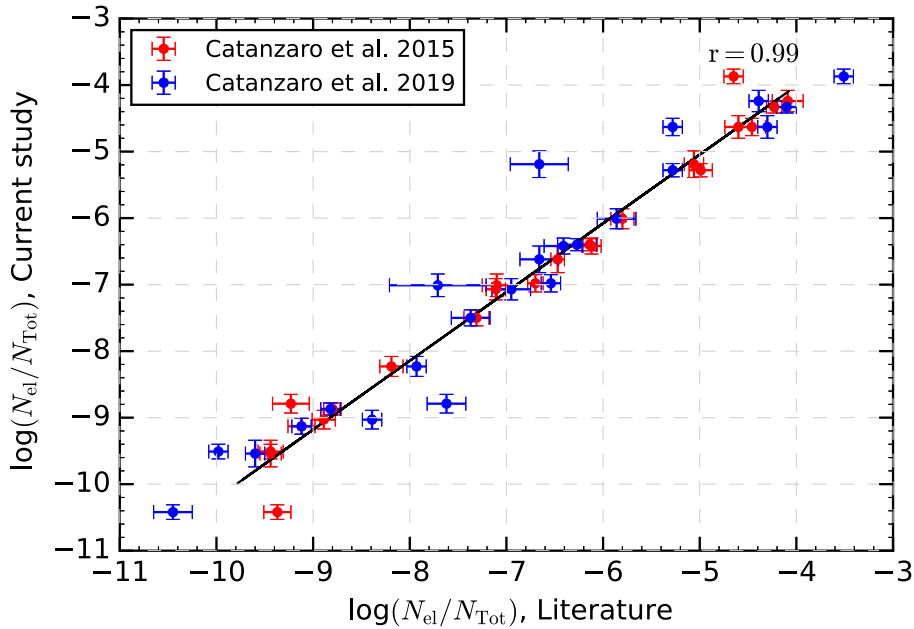


Figure 9. A comparison of our individual chemical abundances with those determined by Catanzaro et al. (2015) and Catanzaro et al. (2019). The corresponding correlation coefficient (r) is given in the top-right corner.

the corresponding lines in HD 180347, of $\Delta \simeq -0.02$ dex and $\Delta < 0.01$ dex for Fe I and Fe II, respectively.

Individual line abundances are presented in Tables 4, 5, 6, and 7. Fig. 11 shows the differences between the LTE and NLTE abundances (Δ) as a function of wavelength. The NLTE effects can be different for the lines produced by the same chemical species. In general, the LTE assumption is valid in deep atmospheric layers where the medium is opaque to the continuum radiation, collisional processes in each atom prevail over radiative ones and the radiation field is close

to the thermodynamic equilibrium. The departures from LTE grow towards the surface, resulting in greater NLTE effects for the strong spectral lines compared with those for the weak lines of the same chemical species. As a rule, the resonance lines and the lines arising from the low-excitation levels are stronger than the remaining lines of the same chemical species. This explains why Δ is larger for Na I 588.9 nm than for Na I 568.8 nm and for Mg II 448.1 nm than for Mg II 438.5 nm. For Mg I, the weaker lines, such as 470.3 and 552.8 nm, are weakened in NLTE due to the ultra-violet overionization, resulting

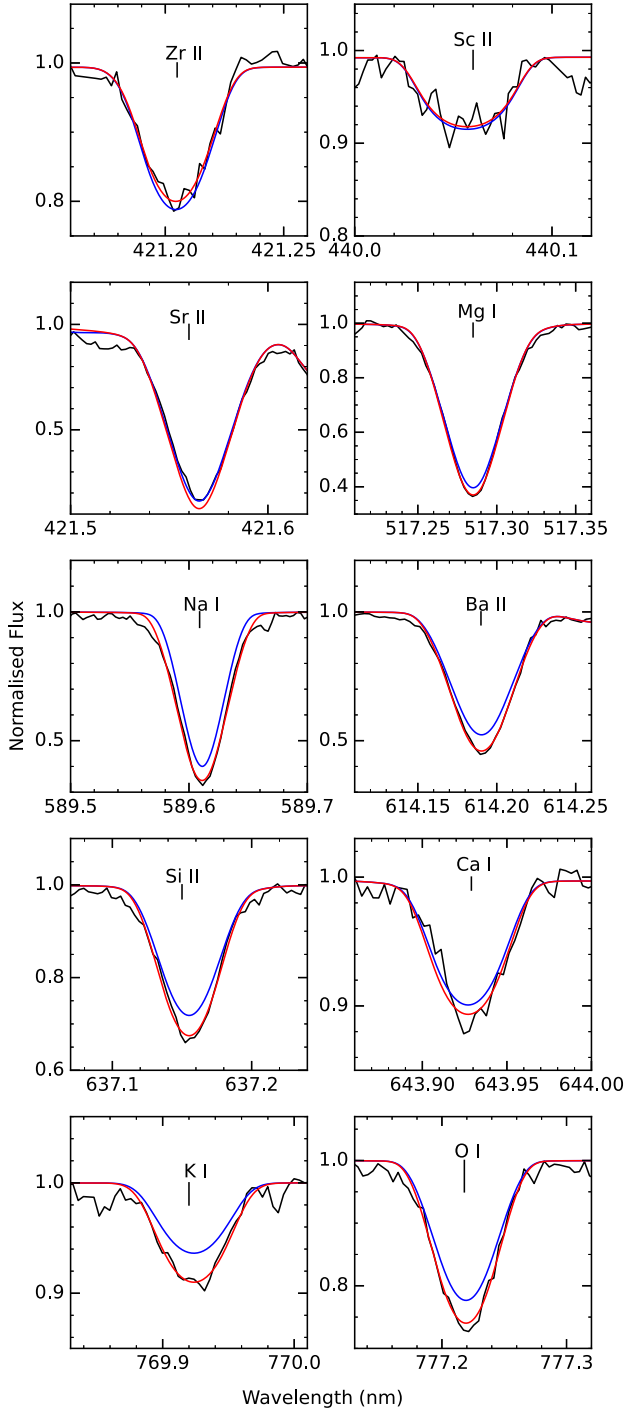


Figure 10. NLTE (red) fits of Zr II 421.188, Sc II 440.039, Sr II 421.552, Mg I 517.285, Na I 589.592, Ba II 614.171, Si II 637.137, Ca I 643.929, K I 769.897, and O I 777.194 nm. For each line, the LTE (blue) profile was computed with the respective abundance obtained from NLTE analysis. In each panel, the black line represents the observed spectrum.

in slightly negative Δ . In contrast, the absorption in the strong Mg I 516.7, 517.2, 518.3 nm lines is larger in NLTE than in LTE, resulting in a positive Δ . An explanation lies within the behaviour of the source function for these strong lines that drops relative to the Planck function in the uppermost atmospheric layers (see Alexeeva et al. 2018 for more details). For Ba II, the NLTE effects

Table 4. Listed are atomic data for O I, Na I, Mg I/II, K I, Sr I, and Ba II lines: the wavelength in nm of the lines used in the analysis, the oscillator strengths ($\log(gf)$) and excitation energy (E_{low}) of the lower level as given in the VALD3 database, the LTE and NLTE abundances, and the abundance correction (Δ). Δ is the difference between LTE and NLTE abundances. LTE means $\log(N_{\text{el}}/N_{\text{Tot}})_{\text{LTE}}$ and NLTE means $\log(N_{\text{el}}/N_{\text{Tot}})_{\text{NLTE}}$.

Wavelength (nm)	$\log(gf)$	E_{low} (eV)	LTE	NLTE	Δ
O I	–	–	–	–	–
777.194	0.369	9.15	–3.78	–4.05	0.27
777.417	0.223	9.15	–3.87	–4.04	0.17
777.539	0.002	9.15	–3.95	–4.07	0.14
Mean	–	–	–3.87	–4.05	0.19
σ	–	–	0.07	0.01	–
Na I	–	–	–	–	–
568.263	–0.706	2.10	–5.13	–5.26	0.13
568.82	–0.452	2.10	–5.33	–5.47	0.14
588.995	0.11	0.0	–4.94	–5.61	0.67
589.592	–0.194	0.0	–4.93	–5.65	0.72
615.423	–1.547	2.10	–5.36	–5.44	0.08
616.075	–1.246	2.10	–5.44	–5.53	0.09
Mean	–	–	–5.19	–5.49	0.31
σ	–	–	0.20	0.13	–
Mg I	–	–	–	–	–
416.727	–0.745	4.35	–4.83	–4.8	–0.03
457.11	–5.623	0.0	–4.66	–4.62	–0.04
470.299	–0.44	4.35	–4.91	–4.9	–0.01
473.003	–2.347	4.35	–4.27	–4.24	–0.03
516.732	–0.931	2.71	–4.56	–4.71	0.15
517.268	–0.45	2.71	–4.69	–4.83	0.14
518.36	–0.239	2.72	–4.37	–4.54	0.17
552.841	–0.498	4.35	–4.89	–4.86	–0.03
571.109	–1.724	4.35	–4.69	–4.65	–0.04
631.875	–2.103	5.11	–4.34	–4.33	–0.01
Mean	–	–	–4.62	–4.65	0.03
σ	–	–	0.22	0.21	–
Mg II	–	–	–	–	–
438.464	–0.79	10.00	–4.6	–4.61	0.01
448.115	1.385	8.86	–4.56	–4.76	0.2
787.705	0.39	10.00	–4.74	–4.81	0.07
789.637	0.69	10.00	–4.75	–4.84	0.09
Mean	–	–	–4.66	–4.76	0.09
σ	–	–	0.08	0.09	–
K I	–	–	–	–	–
769.897	–0.180	0.0	–7.14	–7.35	–0.21
Sr II	–	–	–	–	–
407.771	0.143	0.0	–7.94	–7.98	0.04
416.179	–0.327	2.94	–8.43	–8.36	–0.07
421.552	–0.173	0.0	–8.02	–8.1	0.08
430.544	–0.041	3.04	–8.52	–8.46	–0.06
Mean	–	–	–8.23	–8.23	0.00
σ	–	–	0.25	0.19	–
Ba II	–	–	–	–	–
455.403	0.17	0.0	–8.54	–8.71	0.17
493.408	–0.17	0.0	–8.5	–8.76	0.26
614.171	–0.07	0.7	–8.56	–8.9	0.34
649.69	–0.37	0.6	–8.37	–8.78	0.39
Mean	–	–	–8.49	–8.79	0.29
σ	–	–	0.07	0.07	–

are similarly strong for the resonance lines and the low-excitation lines.

As can be seen in Tables 4, 5, 6, and 7, NLTE reduces the line-to-line scatter and thus the error of the mean abundance for most of the chemical species. This concerns, in particular, Na I and Sr II.

Table 5. Similar to Table 4 but for Ca I/II, Sc II, and Zr II lines.

Wavelength (nm)	log (<i>g</i> f)	E_{low} (eV)	LTE	NLTE	Δ
Ca I	–	–	–	–	–
422.673	0.244	0.0	–6.85	–6.9	0.06
429.899	–0.359	1.89	–6.83	–6.83	0.0
445.478	0.258	1.9	–6.53	–6.56	0.03
452.693	–0.548	2.71	–6.71	–6.79	0.08
457.855	–0.697	2.52	–6.46	–6.41	–0.05
526.224	–0.471	2.52	–7.08	–7.07	–0.01
526.556	–0.113	2.52	–6.36	–6.34	–0.02
527.027	0.162	2.53	–6.32	–6.4	0.08
534.947	–0.31	2.71	–6.63	–6.6	–0.03
551.298	–0.464	2.93	–6.47	–6.45	–0.02
558.197	–0.555	2.52	–6.48	–6.48	0.0
558.875	0.358	2.53	–6.8	–6.81	0.02
559.446	0.097	2.52	–6.46	–6.48	0.01
585.745	0.24	2.93	–6.26	–6.27	0.01
610.272	–0.793	1.88	–6.5	–6.52	0.02
616.644	–1.142	2.52	–6.47	–6.48	0.02
616.905	–0.797	2.52	–6.45	–6.46	0.01
616.956	–0.478	2.53	–6.46	–6.48	0.02
643.908	0.39	2.53	–6.74	–6.78	0.05
644.981	–0.502	2.52	–6.73	–6.77	0.04
646.257	0.262	2.52	–6.57	–6.63	0.06
647.166	–0.686	2.53	–6.56	–6.61	0.05
649.378	–0.109	2.52	–6.75	–6.82	0.07
649.965	–0.818	2.52	–7.13	–7.42	0.29
671.768	–0.524	2.71	–6.49	–6.5	0.01
714.815	0.137	2.71	–6.62	–6.67	0.05
732.615	–0.208	2.93	–6.7	–6.83	0.13
Mean	–	–	–6.61	–6.64	0.04
σ	–	–	0.21	0.24	–
Ca II	–	–	–	–	–
501.997	–0.247	7.51	–6.99	–7.0	0.01
Sc II	–	–	–	–	–
424.682	0.24	0.32	–10.48	–10.46	–0.02
440.039	–0.54	0.61	–10.53	–10.51	–0.02
503.102	–0.41	1.36	–10.26	–10.23	–0.03
552.679	–0.01	1.77	–10.42	–10.4	–0.02
Mean	–	–	–10.42	–10.40	–0.02
σ	–	–	0.10	0.11	–
Zr II	–	–	–	–	–
404.867	–0.53	0.80	–8.8	–8.76	–0.04
415.628	–0.776	0.71	–8.81	–8.8	–0.01
420.898	–0.51	0.71	–9.14	–9.1	–0.04
421.188	–1.04	0.53	–8.86	–8.81	–0.05
449.696	–0.89	0.71	–8.86	–8.82	–0.04
511.227	–0.85	1.66	–8.75	–8.72	–0.03
Mean	–	–	–8.87	–8.84	–0.04
σ	–	–	0.13	0.12	–

For the elements important for identification of the star’s chemical peculiarity, NLTE supports the conclusions deduced from the LTE analysis but improves the magnitudes of the abundance deviations: O, Ca, and Sc are strongly depleted relative to their solar abundances, with $[\text{O}/\text{H}]_{\text{NLTE}} = -0.7$ dex, $[\text{Ca}/\text{H}]_{\text{NLTE}} = -0.96$ dex, and $[\text{Sc}/\text{H}]_{\text{NLTE}} = -1.51$ dex, while Sr, Zr, and Ba are enhanced, with $[\text{X}/\text{H}] > 0.7$ dex. We note that potassium, with $[\text{K}/\text{H}]_{\text{NLTE}} = -0.34$ dex, falls short of solar abundance. NLTE reduces the overabundances of Na and Si obtained in LTE.

To the best of our knowledge, the NLTE abundance analyses are available in the literature for three Am stars. For a nascent Am star HD 131399A ($T_{\text{eff}} = 9200$ K, $\log g = 4.37$ cm s^{–2}), Przybilla,

Table 6. Similar to Table 4 but for Si I/II lines.

Wavelength (nm)	log (<i>g</i> f)	E_{low} (eV)	LTE	NLTE	Δ
Si I	–	–	–	–	–
551.753	–2.61	5.08	–4.67	–4.68	0.01
562.222	–2.606	4.93	–4.52	–4.44	–0.08
564.561	–2.14	4.93	–4.27	–4.3	0.03
566.555	–2.04	4.92	–4.15	–4.18	0.03
569.043	–1.87	4.93	–4.22	–4.25	0.03
570.11	–2.05	4.93	–4.04	–4.07	0.03
570.84	–1.47	4.95	–4.15	–4.19	0.04
577.215	–1.75	5.08	–4.17	–4.19	0.02
594.854	–1.23	5.08	–4.25	–4.28	0.03
608.781	–1.815	5.87	–3.99	–4.02	0.03
612.502	–1.465	5.61	–4.13	–4.15	0.02
614.248	–1.296	5.62	–4.41	–4.43	0.02
614.502	–1.311	5.62	–4.29	–4.32	0.03
615.513	–0.755	5.62	–4.44	–4.46	0.02
623.732	–0.975	5.61	–4.42	–4.44	0.02
624.382	–1.244	5.62	–4.32	–4.34	0.02
624.447	–1.091	5.62	–4.4	–4.43	0.03
641.498	–1.036	5.87	–4.23	–4.27	0.04
672.185	–1.527	5.86	–3.9	–3.93	0.03
684.858	–1.528	5.86	–4.17	–4.19	0.02
697.651	–1.17	5.95	–4.05	–4.08	0.03
700.357	–0.89	5.96	–4.15	–4.18	0.03
700.588	–0.69	5.98	–4.25	–4.28	0.03
703.49	–0.88	5.87	–4.19	–4.22	0.03
722.621	–1.51	5.61	–4.25	–4.25	0.0
723.533	–1.49	5.62	–4.0	–4.03	0.03
737.3	–1.18	5.98	–4.13	–4.17	0.04
740.577	–0.82	5.61	–4.19	–4.25	0.06
741.536	–1.76	5.62	–4.14	–4.18	0.04
742.35	–0.176	5.62	–4.75	–4.82	0.07
784.997	–0.714	6.19	–4.18	–4.21	0.03
791.838	–0.61	5.95	–4.29	–4.33	0.04
793.235	–0.47	5.96	–4.21	–4.25	0.04
794.4	–0.31	5.98	–4.2	–4.27	0.07
797.031	–1.47	5.96	–3.95	–3.99	0.04
Mean	–	–	–4.23	–4.26	–0.03
σ	–	–	0.18	0.17	–
Si II	–	–	–	–	–
412.805	0.41	9.84	–4.68	–4.69	0.01
462.172	–0.38	12.53	–4.23	–4.21	–0.02
505.632	0.53	10.07	–4.34	–4.37	0.03
595.756	–0.26	10.07	–4.12	–4.14	0.02
597.893	0.04	10.07	–4.37	–4.4	0.03
634.711	0.17	8.12	–4.18	–4.52	0.34
637.137	–0.04	8.12	–4.29	–4.55	0.26
Mean	–	–	–4.32	–4.41	0.1
σ	–	–	0.17	0.18	–

Aschenbrenner & Buder (2017) determined the NLTE abundances of He, C, N, O, Mg, Si, Ti, and Fe. In contrast to our target, HD 131399A does not reveal any underabundances of C, O, Ca, and Sc, probably, due to its young age (16 Myr). Although Ca and Sc were treated under the LTE assumption, the NLTE effects are not expected to reduce their abundances to the level observed in HD 180347. Common for HD 131399A and our target is a substantial enhancement in Sr, Zr, and Ba. For $T_{\text{eff}}/\log g$ of HD 131399A, NLTE is expected to increase abundances of these elements to an even higher level. For a benchmark Am star Sirius (HD 48915, $T_{\text{eff}} = 9850$ K, $\log g = 4.30$ cm s^{–2}) and an Am star HD 72 660 with close atmospheric

Table 7. Similar to Table 4 but for C I, Ti I/II, and Zn I lines. The NLTE abundances are obtained by adding the NLTE abundance corrections predicted by Alexeeva et al. (2016), Sitnova et al. (2016), and Sitnova et al. (2022) for lines C I, Ti I–II, and Zn I, respectively.

Wavelength (nm)	log (<i>g</i> f)	E_{low} (eV)	LTE	NLTE	Δ
C I					
476.666	−2.617	7.48	−3.88	−3.92	0.04
477.002	−2.437	7.48	−4.4	−4.44	0.04
477.589	−2.304	7.49	−4.25	−4.29	0.04
601.483	−1.584	8.64	−4.19	−4.21	0.02
711.146	−1.09	8.64	−4.3	−4.34	0.04
711.517	−0.93	8.64	−4.47	−4.51	0.04
711.965	−1.148	8.64	−4.32	−4.36	0.04
Mean	−	−	−4.26	−4.30	0.04
σ	−	−	0.18	0.18	−
Ti I					
428.74	−0.37	0.84	−7.67	−7.59	−0.08
451.273	−0.4	0.84	−6.94	−6.86	−0.08
453.324	0.54	0.85	−7.0	−6.92	−0.08
453.478	0.35	0.84	−7.48	−7.4	−0.08
454.876	−0.28	0.83	−7.15	−7.07	−0.08
461.727	0.44	1.75	−7.2	−7.07	−0.13
475.927	0.59	2.26	−7.3	−7.21	−0.09
498.173	0.57	0.85	−7.27	−7.22	−0.05
499.95	0.32	0.83	−6.87	−6.81	−0.06
501.616	−0.48	0.85	−7.2	−7.13	−0.07
502.557	0.25	2.04	−6.88	−6.8	−0.08
503.646	0.14	1.44	−7.09	−7.01	−0.08
517.374	−1.06	0.0	−6.93	−6.79	−0.14
519.297	−0.95	0.02	−6.71	−6.57	−0.14
521.038	−0.82	0.05	−6.99	−6.85	−0.14
Mean	−	−	−7.11	−7.02	−0.09
σ	−	−	0.24	0.25	−
Ti II					
402.834	−0.92	1.89	−7.23	−7.26	0.03
405.382	−1.07	1.89	−7.38	−7.4	0.02
416.153	−2.09	1.08	−7.08	−7.09	0.01
416.364	−0.13	2.59	−7.12	−7.17	0.05
417.407	−1.26	2.6	−7.29	−7.29	0.0
419.023	−3.122	1.08	−6.96	−6.96	0.0
428.787	−1.79	1.08	−6.98	−7.02	0.04
429.022	−0.87	1.16	−7.1	−7.18	0.08
430.005	−0.46	1.18	−6.82	−6.92	0.1
438.684	−0.96	2.6	−7.08	−7.1	0.02
439.102	−2.3	1.23	−6.72	−6.73	0.01
439.406	−1.77	1.22	−7.34	−7.36	0.02
439.503	−0.54	1.08	−7.18	−7.31	0.13
439.584	−1.93	1.24	−7.28	−7.29	0.01
439.977	−1.2	1.24	−7.2	−7.26	0.06
440.924	−2.78	1.24	−6.82	−6.82	0.0
440.952	−2.53	1.23	−6.89	−6.89	0.0
441.107	−0.65	3.09	−7.1	−7.11	0.01
441.193	−2.62	1.22	−6.95	−6.95	0.0
441.771	−1.19	1.16	−7.3	−7.39	0.09
441.833	−1.99	1.24	−7.21	−7.22	0.01
442.194	−1.64	2.06	−7.11	−7.12	0.01
444.173	−2.33	1.18	−7.17	−7.18	0.01
444.38	−0.71	1.08	−7.21	−7.33	0.12
445.048	−1.52	1.08	−6.87	−6.92	0.05
446.445	−1.81	1.16	−7.19	−7.22	0.03
446.85	−0.63	1.13	−7.11	−7.2	0.09
446.915	−2.55	1.08	−6.91	−6.91	0.0
447.085	−2.02	1.16	−7.21	−7.23	0.02
448.832	−0.5	3.12	−7.18	−7.19	0.01
450.127	−0.77	1.12	−7.11	−7.23	0.12

Table 7 – *continued*

Wavelength (nm)	log (<i>g</i> f)	E_{low} (eV)	LTE	NLTE	Δ
Ti II					
451.833	−2.56	1.08	−7.12	−7.12	0.0
452.947	−1.75	1.57	−7.1	−7.12	0.02
453.396	−0.53	1.24	−7.13	−7.29	0.16
454.402	−2.58	1.24	−7.15	−7.15	0.0
454.962	−0.22	1.58	−6.89	−7.04	0.15
456.376	−0.795	1.22	−7.27	−7.42	0.15
456.831	−3.03	1.22	−7.02	−7.03	0.01
457.197	−0.31	1.57	−6.8	−6.94	0.14
458.341	−2.84	1.16	−7.01	−7.02	0.01
458.996	−1.62	1.24	−7.25	−7.3	0.05
463.632	−3.024	1.24	−7.15	−7.15	0.0
465.72	−2.29	1.24	−6.92	−6.93	0.01
470.866	−2.35	1.24	−7.23	−7.24	0.01
471.952	−3.32	1.24	−6.93	−6.94	0.01
476.388	−2.4	1.22	−6.8	−6.8	0.0
476.453	−2.69	1.24	−6.96	−6.96	0.0
477.999	−1.26	3.28	−7.28	−7.31	0.03
479.853	−2.66	1.08	−7.29	−7.29	0.0
480.509	−0.96	2.06	−7.23	−7.29	0.06
491.119	−0.64	3.12	−7.26	−7.26	0.0
500.516	−2.73	1.57	−7.07	−7.08	0.01
501.021	−1.35	3.09	−7.06	−7.06	0.0
501.333	−2.028	3.09	−6.91	−6.91	0.0
501.369	−2.14	1.58	−7.18	−7.19	0.01
507.229	−1.02	3.12	−6.89	−6.9	0.01
512.916	−1.34	1.89	−6.77	−6.81	0.04
515.407	−1.75	1.57	−7.19	−7.23	0.04
518.591	−1.41	1.89	−7.27	−7.3	0.03
521.154	−1.41	2.59	−7.2	−7.21	0.01
526.861	−1.61	2.6	−7.04	−7.04	0.0
533.679	−1.6	1.58	−7.21	−7.25	0.04
538.102	−1.97	1.57	−7.1	−7.12	0.02
541.877	−2.13	1.58	−7.17	−7.19	0.02
668.013	−1.89	3.09	−7.02	−7.03	0.01
699.891	−1.28	3.12	−6.99	−7.01	0.02
Mean	−	−	−7.09	−7.12	0.03
σ	−	−	0.16	0.16	−
Zn I					
4722.153	−0.338	4.03	−6.92	−6.86	−0.06
4810.528	−0.137	4.08	−7.04	−6.98	−0.06
Mean	−	−	−6.98	−6.92	−0.06
σ	−	−	0.06	0.06	−

parameters ($T_{\text{eff}} = 9700$ K, $\log g = 4.10$ cm s $^{-2}$), Mashonkina et al. (2020) derived the NLTE abundances of He, C, O, Na, Mg, Si, Ca, Ti, Fe, Sr, Zr, Ba, and Nd. Mashonkina et al. (2020) note a rather different behaviour of Ca and Sc in their two stars, namely, Ca is slightly depleted and Sc is strongly depleted in Sirius, while Ca is enhanced and Sc is moderately depleted in HD 72660. Despite Sc being treated in LTE, the NLTE effects are expected to be similar for these two stars with similar atmospheric parameters. Both stars reveal enhancements in the heavy elements (Sr to Nd) at a level similar to that for our target or the higher level.

7 CONCLUSION

Catanzaro et al. (2019) suspected that HD 180347 had δ Scuti-type pulsations. Based on the diffusion theory, such pulsations are unexpected given that it is a candidate Am star. Therefore, the photometric variability and chemical nature of HD 180347 are

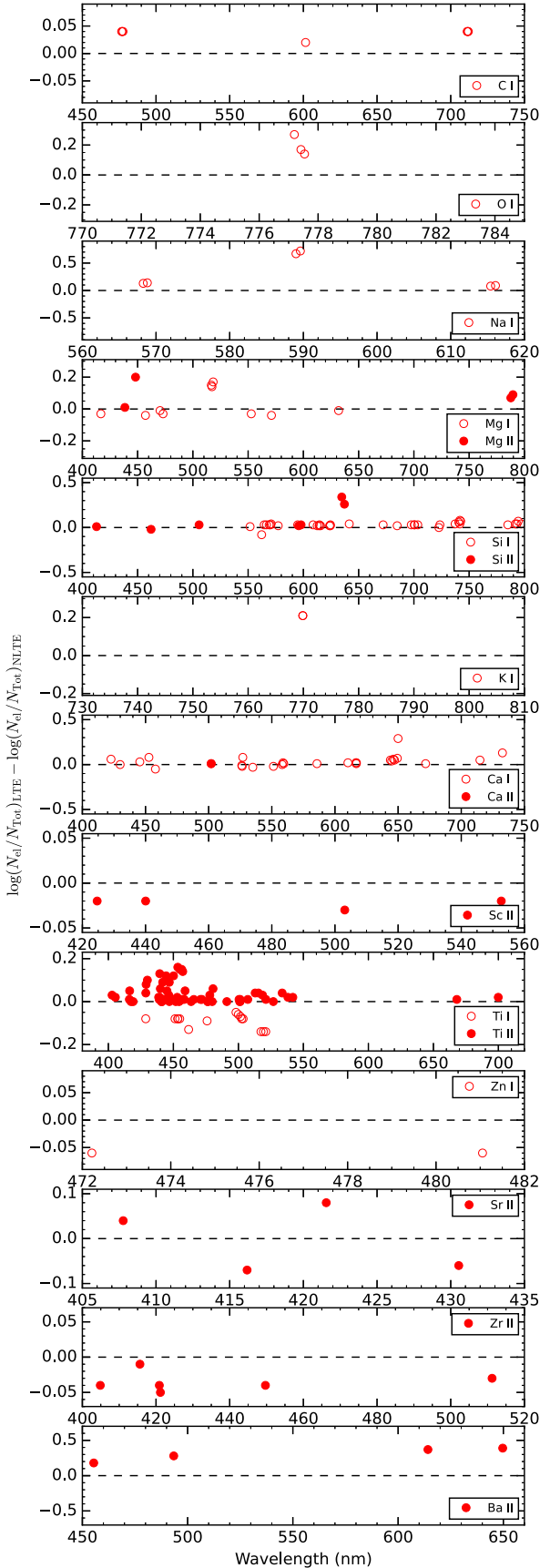


Figure 11. Abundance differences between the LTE and NLTE analyses for Na I, Mg I/II, Si I/II, Ca I/II, Sr II, and Ba II.

investigated in detail in this study. The analysis is based on high-precision photometric data by *TESS* and a high-resolution spectrum obtained with HERMES mounted at the Cassegrain focus of the 1.2-m Mercator telescope located at La Palma, Spain. This study increases the statistics of Am stars with accurate NLTE abundances derived for important chemical elements. Knowledge of the abundance anomalies depending on stellar parameters should play a key role in understanding the mechanisms of the chemical peculiarities of Am stars.

We searched for the variability type, determined the spectral type, and obtained fundamental parameters such as the effective temperature, surface gravity, and projected rotational, microturbulent, and radial velocity. Based on these results, we estimated the radius, equatorial rotational velocity, inclination angle, mass, and age of HD 180347. Finally, we performed a detailed chemical abundance analysis.

Based on the variability analysis of the high-precision photometric data by *TESS* (sectors 14, 15, and 26), we classify HD 180347 as a rotational variable with a period of 4.1 ± 0.2 d. In reference to the observation limit of *TESS*, no pulsations were detected as previously suspected by Catanzaro et al. (2019). The rotational amplitude of 0.08 mmag indicates significant spots and thus potentially significant magnetic fields. A spectropolarimetric analysis of this star is required to estimate its magnetic field strength.

We calculated LTE abundances for 25 different chemical elements. We also report the non-local thermodynamic equilibrium (NLTE) abundances for 13 of them, including Ca, Sc, Sr, Zr, and Ba, which are significant for the characterization of chemical peculiarity. The use of NLTE increases the accuracy of the derived abundances and indicates that Ca and Sc are depleted in HD 180347 relative to their solar abundances, while heavy elements beyond Sr are increased by more than 0.7 dex. Based on the spectral classification analysis and chemical abundance pattern, we classified this star as Am (kA1hA8mA8).

The availability of HERMES and other spectrographs capable of high-resolution spectroscopy will allow us, in future, to continue with the study of A and probable Am stars especially those reported in Renson & Manfroid (2009). Efforts will be made to increase the number of elements in NLTE abundance analyses.

ACKNOWLEDGEMENTS

The International Science Program (ISP) of Uppsala University and the African Astronomical Society (AfAS) financed the study. The part of the work presented here is supported by the Belgo-Indian Network for Astronomy & Astrophysics (BINA), approved by the International Division, Department of Science and Technology (DST, Govt. of India; DST/INT/Belg/P09/2017) and the Belgian Federal Science Policy Office (BELSPO, Govt. of Belgium; BL/33/IN12). SJ acknowledges the financial support received from the BRICS grant DST/IC/BRICS/2023/5. We thank Dr Yves Frémat for kindly providing the GIRFIT code. The authors acknowledge the anonymous reviewer for his/her careful reading of our manuscript and for many insightful comments and suggestions which improved the paper. Based on observations obtained with the HERMES spectrograph, which is supported by the Research Foundation – Flanders (FWO), Belgium, the Research Council of KU Leuven, Belgium, the Fonds National de la Recherche Scientifique (F.R.S.-FNRS), Belgium, the Royal Observatory of Belgium, the Observatoire de Genève, Switzerland and the Thüringer Landessternwarte Tautenburg, Germany. This publication makes use of VOSA, developed under the Spanish Virtual Observatory project supported by the Spanish

MINECO through grant AyA2017-84089. VOSA has been partially updated by using funding from the European Union's Horizon 2020 Research and Innovation Programme, under Grant Agreement 776403 (EXOPLANETS-A). This work has made use of the VALD data base, operated at Uppsala University, the Institute of Astronomy RAS in Moscow, and the University of Vienna.

DATA AVAILABILITY

The data underlying this article will be shared on reasonable request to the corresponding author.

REFERENCES

- Abt H. A., 2009, *AJ*, 138, 28
- Aigrain S. et al., 2015, *MNRAS*, 450, 3211
- Alexeeva S., Pakhomov Y., Mashonkina L., 2014, *Astron. Lett.*, 40, 406
- Alexeeva S. A., Ryabchikova T. A., Mashonkina L. I., 2016, *MNRAS*, 462, 1123
- Alexeeva S., Ryabchikova T., Mashonkina L., Hu S., 2018, *ApJ*, 866, 153
- Andrae R. et al., 2018, *A&A*, 616, A8
- Andrae R. et al., 2022, *A&A*, 674, A27
- Ashoka B. N. et al., 2000, *Bull. Astron. Soc. India*, 28, 251
- Asplund M., Grevesse N., Sauval A. J., Scott P., 2009, *ARA&A*, 47, 481
- Aurière M. et al., 2007, *A&A*, 475, 1053
- Balona L. A., Catanzaro G., Abedigamba O. P., Ripepi V., Smalley B., 2015, *MNRAS*, 448, 1378
- Bayo A., Rodrigo C., Barrado Y Navascués D., Solano E., Gutiérrez R., Morales-Calderón M., Allard F., 2008, *A&A*, 492, 277
- Bidelman W. P., 1985, *AJ*, 90, 341
- Blanco-Cuaresma S., 2019, *MNRAS*, 486, 2075
- Blanco-Cuaresma S., Soubiran C., Heiter U., Jofré P., 2014, *A&A*, 569, A111
- Blomme R. et al., 2022, *A&A*, 674, A7
- Bohlender D. A., Dworetzky M. M., Jomaron C. M., 1998, *ApJ*, 504, 533
- Boltzmann L., 1884, *Ann. Phys., Lpz.*, 258, 291
- Borucki W. J. et al., 2010, *Science*, 327, 977
- Bowman D. M., Buyschaert B., Neiner C., Pápics P. I., Oksala M. E., Aerts C., 2018, *A&A*, 616, A77
- Breger M. et al., 1993, *A&A*, 271, 482
- Bressan A., Marigo P., Girardi L., Salasnich B., Dal Cero C., Rubele S., Nanni A., 2012, *MNRAS*, 427, 127
- Browning M. K., Brun A. S., Toomre J., 2004, *ApJ*, 601, 512
- Butler K., 1984, Ph.D. Thesis, University of London
- Castelli F., Kurucz R. L., 2003, in Piskunov N., Weiss W. W., Gray D. Feds, IAU Symp. Vol. 210, Modelling of Stellar Atmospheres. Cambridge University Press, Cambridge, p. A20
- Catanzaro G. et al., 2015, *MNRAS*, 451, 184
- Catanzaro G., Busà I., Gangi M., Giarrusso M., Leone F., Munari M., 2019, *MNRAS*, 484, 2530
- Ceillier T. et al., 2016, *MNRAS*, 456, 119
- Ceillier T. et al., 2017, *A&A*, 605, A111
- Conti P. S., 1970, *PASP*, 82, 781
- Costa G., Girardi L., Bressan A., Marigo P., Rodrigues T. S., Chen Y., Lanza A., Goudfrooij P., 2019, *MNRAS*, 485, 4641
- Dziembowski W., Krolikowska M., Kosovichev A., 1988, *AcA*, 38, 61
- Evans D. W. et al., 2018, *A&A*, 616, A4
- Flower P. J., 1996, *ApJ*, 469, 355
- Fossati L., Bagnulo S., Landstreet J., Wade G., Kochukhov O., Monier R., Weiss W., Gebran M., 2008, *A&A*, 483, 891
- Frémat Y., Neiner C., Hubert A. M., Floquet M., Zorec J., Janot-Pacheco E., Renan de Medeiros J., 2006, *A&A*, 451, 1053
- Frescura F. A. M., Engelbrecht C. A., Frank B. S., 2008, *MNRAS*, 388, 1693
- García R. A., Mathur S., Salabert D., Ballot J., Régulo C., Metcalfe T. S., Baglin A., 2010, *Science*, 329, 1032
- Gebran M., Monier R., Royer F., Lobel A., Blomme R., 2014, in Mathys G., Griffin E. R., Kochukhov O., Monier R., Wahlgren G. M.eds, Putting A Stars into Context: Evolution, Environment, and Related Stars. Pero, Moscow, Russia, p. 193
- Giddings J., 1981, Ph.D. Thesis, University of London
- Giles H. A. C., Collier Cameron A., Haywood R. D., 2017, *MNRAS*, 472, 1618
- Goupillaud P., Grossmann A., Morlet J., 1984, *Geoploration*, 23, 85
- Gray R. O., Corbally Christopher J., 2009, *Stellar Spectral Classification*. Princeton University Press, Princeton
- Gray R. O., Corbally C. J., 2014, *AJ*, 147, 80
- Gray R. O., Corbally C. J., Garrison R. F., McFadden M. T., Robinson P. E., 2003, *AJ*, 126, 2048
- Green G. M., 2018, *JOSS*, 3, 695
- Green G. M., Schlafly E., Zucker C., Speagle J. S., Finkbeiner D., 2019, *ApJ*, 887, 93
- Holschneider M., Kronland-Martinet R., Morlet J., Tchamitchian P., 1989, in Combes J.-M., Grossmann A., Tchamitchian Peds, Wavelets. Time-Frequency Methods and Phase Space. Springer-Verlag, Berlin
- Hui-Bon-Hoa A., 2000, *A&AS*, 144, 203
- Jenkins J. M. et al., 2016, in G. Chiozzi, C. Guzman J.eds, SPIE Conf. Ser. Vol. 9913, Software and Cyberinfrastructure for Astronomy IV, p. 99133E
- Jones T. J., Wolff S. C., 1974, *PASP*, 86, 67
- Jönsson H. et al., 2020, *AJ*, 160, 120
- Joshi S. et al., 2003, *MNRAS*, 344, 431
- Joshi S., Mary D. L., Martinez P., Kurtz D. W., Girish V., Seetha S., Sagar R., Ashoka B. N., 2006, *A&A*, 455, 303
- Joshi S., Mary D. L., Chakradhari N. K., Tiwari S. K., Billaud C., 2009, *A&A*, 507, 1763
- Joshi S., Ryabchikova T., Kochukhov O., Sachkov M., Tiwari S. K., Chakradhari N. K., Piskunov N., 2010, *MNRAS*, 401, 1299
- Joshi S. et al., 2012, *MNRAS*, 424, 2002
- Joshi S. et al., 2016, *A&A*, 590, A116
- Joshi S., Semenko E., Moiseeva A., Sharma K., Joshi Y. C., Sachkov M., Singh H. P., Yerra B. K., 2017, *MNRAS*, 467, 633
- Joshi S. et al., 2022, *MNRAS*, 510, 5854
- Kazarovets E., Durlevich O., Kireeva N., Pastukhova E. et al., 2017, *Astron. Rep.*, 61, 80
- Khokhlova V. L., 1981, *Liege International Astrophysical Colloquia*. Vol. 23, p.457
- Kochukhov O., 2018, *BinMag: Widget for comparing stellar observed with theoretical spectra Astrophysics Source Code Library*, record(asc1:1805.015)
- Koen C., 2010, *Ap&SS*, 329, 267
- Kupka F., Piskunov N., Ryabchikova T. A., Stempels H. C., Weiss W. W., 1999, *A&AS*, 138, 119
- Kurtz D. W., Martinez P., 2000, *BaltA*, 9, 253
- LaSala J., 1994, in Corbally C. J., Gray R. O., Garrison R. F.eds, ASP Conf. Ser. Vol. 60, The MK Process at 50 Years: A Powerful Tool for Astrophysical Insight. Astron. Soc. Pac., San Francisco, p. 312
- Lampton M., Margon B., Bowyer S., 1976, *ApJ*, 208, 177
- Lenz P., Breger M., 2005, *CoAst*, 146, 53
- Martinez P. et al., 2001, *A&A*, 371, 1048
- Mashonkina L., 2020, *MNRAS*, 493, 6095
- Mashonkina L. I., Romanovskaya A. M., 2022, *Astron. Lett.*, 48, 455
- Mashonkina L., Korn A. J., Przybilla N., 2007, *A&A*, 461, 261
- Mashonkina L., Ryabchikova T., Alexeeva S., Sitnova T., Zatsarinny O., 2020, *MNRAS*, 499, 3706
- Mathur S. et al., 2010, *A&A*, 511, A46
- Mathur S. et al., 2014, *A&A*, 562, A124
- Mathur S. et al., 2017, *ApJS*, 229, 30
- McDonald I., Zijlstra A. A., Boyer M. L., 2012, *MNRAS*, 427, 343
- McQuillan A., Aigrain S., Mazeh T., 2013, *MNRAS*, 432, 1203
- McQuillan A., Mazeh T., Aigrain S., 2014, *ApJS*, 211, 24
- Michaud G., 1970, *ApJ*, 160, 641
- Montambaux G., 2018, *Found. Phys.*, 48, 395
- Morgan W. W., Keenan P. C., Kellman E., 1943, *An atlas of stellar spectra, with an outline of spectral classification*. The University of Chicago press, Chicago

- Murphy S. J., 2014, PhD thesis, Jeremiah Horrocks Institute, University of Central Lancashire, Preston, UK <EMAIL>murphy@physics.usyd.edu.au</EMAIL>
- Murphy S. J., Hey D., Van Reeth T., Bedding T. R., 2019, *MNRAS*, 485, 2380
- Narlikar J., 1995, *From Black Clouds to Black Holes. Series in Astronomy and Astrophysics*, World Scientific, 2nd, <https://doi.org/10.1142/2541>
- Neretina M. D., Mashonkina L. I., Sitnova T. M., Yakovleva S. A., Belyaev A. K., 2020, *Astron. Lett.*, 46, 621
- Paul H., Greenberger D. M., Stenholm S. T., Schleich W. P., 2015, *Phys. Scr.T*, T165, 014027
- Preston G. W., 1974, *ARA&A*, 12, 257
- Przybilla N., Nieva M.-F., Butler K., 2011 *J. Phys. Conf. Ser.*, 328, 012015
- Przybilla N., Aschenbrenner P., Buder S., 2017, *A&A*, 604, L9
- Raskin G. et al., 2011, *A&A*, 526, A69
- Renson P., Manfroid J., 2009, *A&A*, 498, 961
- Richer J., Michaud G., Turcotte S., 2000, *ApJ*, 529, 338
- Ricker G. R. et al., 2015, *JATIS*, 1, 014003
- Romanyuk I. I., 2007, *Astrophys. Bull.*, 62, 62
- Ryabchikova T., Piskunov N., Kurucz R. L., Stempels H. C., Heiter U., Pakhomov Y., Barklem P. S., 2015, *Phys. Scr.*, 90, 054005
- Rybicki G. B., Hummer D. G., 1991, *A&A*, 245, 171
- Rybicki G. B., Hummer D. G., 1992, *A&A*, 262, 209
- Shulyak D., Tsymbal V., Ryabchikova T., Stütz C., Weiss W. W., 2004, *A&A*, 428, 993
- Sitnova T. M., Mashonkina L. I., Ryabchikova T. A., 2013, *Astron. Lett.*, 39, 126
- Sitnova T. M., Mashonkina L. I., Ryabchikova T. A., 2016, *MNRAS*, 461, 1000
- Sitnova T. M., Yakovleva S. A., Belyaev A. K., Mashonkina L. I., 2022, *MNRAS*, 515, 1510
- Smalley B. et al., 2011, *A&A*, 535, A3
- Smith K. C., 1997, *A&A*, 319, 928
- Snedden C., Bean J., Ivans I., Lucatello S., Sobek J., 2012, MOOG: LTE line analysis and spectrum synthesis, Astrophysics Source Code Library strophysics Source Code Library, record (ascl:1202.009)
- Soufi F., Goupil M. J., Dziembowski W. A., 1998, *A&A*, 334, 911
- Stateva I. K., Iliev I. K., Budaj J., Barzova I. S., 2009, *BAJ*, 12, 29
- Takeda Y., Han I., Kang D.-I., Lee B.-C., Kim K.-M., 2008, *J. Korean Astron. Soc.*, 41, 83
- Théado S., Vauclair S., Alecian G., LeBlanc F., 2011, in Alecian G., Belkacem K., Samadi R., Valls-Gabaud D., eds, SF2A-2011: Proceedings of the Annual meeting of the French Society of Astronomy and Astrophysics. p. 253
- Torrence C., Compo G. P., 1998, *Bull. Am. Meteorol. Soc.*, 79, 61
- Torres G., 2010, *AJ*, 140, 1158
- Trust O., Jurua E., De Cat P., Joshi S., 2020, *MNRAS*, 492, 3143
- Trust O., Jurua E., De Cat P., Joshi S., Lampens P., 2021, *MNRAS*, 504, 5528
- Tsymbal V., Ryabchikova T., Sitnova T., 2019, in Kudryavtsev D. O., Romanyuk I. I., Yakunin I. A. eds, ASP Conf. Ser. Vol. 518, Physics of Magnetic Stars. Astron. Soc. Pac., San Francisco, p. 247
- Turcotte S., 2002, *ASP Conf. Ser. Vol. 259, IAU Colloq. 185: Radial and Nonradial Pulsations as Probes of Stellar Physics*, Astron. Soc. Pac., San Francisco, p. 258
- Turcotte S., 2003, in Balona L. A., Henrichs H. F., Medupe R. eds, ASP Conf. Ser. Vol. 305, Magnetic Fields in O, B and A Stars: Origin and Connection to Pulsation, Rotation and Mass Loss. Astron. Soc. Pac., San Francisco, p. 199
- VanderPlas J. T., 2018, *ApJS*, 236, 16
- Watson W. D., 1970, *ApJL*, 162, L45
- Wenger M. et al., 2000, *A&AS*, 143, 9

This paper has been typeset from a $\text{\TeX}/\text{\LaTeX}$ file prepared by the author.